

PAPER • OPEN ACCESS

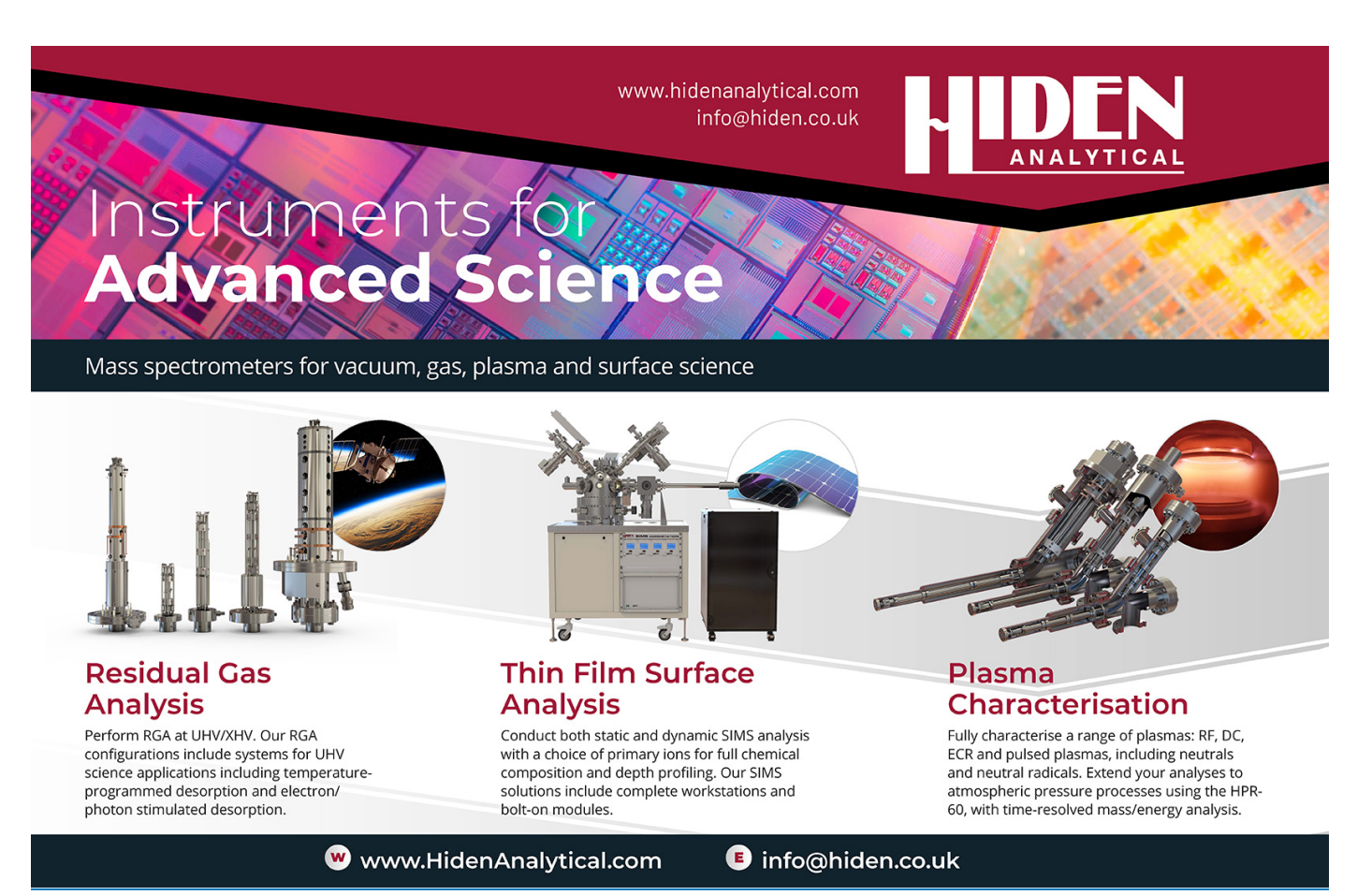
Dynamically generated decoherence-free subspaces and subsystems on superconducting qubits

To cite this article: Gregory Quiroz et al 2024 Rep. Prog. Phys. 87 097601

View the article online for updates and enhancements.

You may also like

- Molecular nanomagnets: a viable path toward quantum information processing?
 A Chiesa, P Santini, E Garlatti et al.
- Mechanical, electronic, optical, piezoelectric and ferroic properties of strained graphene and other strained monolayers and multilayers: an update Gerardo G Naumis, Saúl A Herrera, Shiva P Poudel et al.
- Many-body localization in the age of classical computing Piotr Sierant, Maciej Lewenstein, Antonello Scardicchio et al.



Rep. Prog. Phys. 87 (2024) 097601 (25pp)

https://doi.org/10.1088/1361-6633/ad6805

Dynamically generated decoherence-free subspaces and subsystems on superconducting qubits

Gregory Quiroz^{1,2,*}, Bibek Pokharel^{3,4,11}, Joseph Boen¹, Lina Tewala^{1,5}, Vinay Tripathi^{3,4}, Devon Williams^{1,2}, Lian-Ao Wu^{6,7,8}, Paraj Titum¹, Kevin Schultz¹ and Daniel Lidar^{3,4,9,10}

E-mail: Gregory.Quiroz@jhuapl.edu

Received 15 March 2024, revised 12 June 2024 Accepted for publication 15 July 2024 Published 14 August 2024

Corresponding editor: Dr Lorna Brigham



Abstract

Decoherence-free subspaces and subsystems (DFS) preserve quantum information by encoding it into symmetry-protected states unaffected by decoherence. An inherent DFS of a given experimental system may not exist; however, through the use of dynamical decoupling (DD), one can induce symmetries that support DFSs. Here, we provide the first experimental demonstration of DD-generated decoherence-free subsystem logical qubits. Utilizing IBM Quantum superconducting processors, we investigate two and three-qubit DFS codes comprising up to six and seven noninteracting logical qubits, respectively. Through a combination of DD and error detection, we show that DFS logical qubits can achieve up to a 23% improvement in state preservation fidelity over physical qubits subject to DD alone.

¹¹ Currently at IBM Quantum, Almaden Research Center, San Jose, CA 95120, United States of America. Author to whom any correspondence should be addressed.



Original Content from this work may be used under the terms of the Creative Commons Attribution 4.0 licence. Any

further distribution of this work must maintain attribution to the author(s) and the title of the work, journal citation and DOI.

¹ Johns Hopkins University Applied Physics Laboratory, Laurel, MD 20723, United States of America

² William H. Miller III Department of Physics & Astronomy, Johns Hopkins University, Baltimore, MD 21218, United States of America

³ Department of Physics and Astronomy, University of Southern California, Los Angeles, CA 90089, United States of America

⁴ Center for Quantum Information Science & Technology, University of Southern California, Los Angeles, CA 90089, United States of America

⁵ Thomas C. Jenkins Department of Biophysics, Johns Hopkins University, Baltimore, MD 21218, United States of America

⁶ Department of Theoretical Physics and History of Science, University of the Basque Country, Leioa 48008, Spain

⁷ IKERBASQUE, Basque Foundation for Science, Bilbao 48011, Spain

⁸ EHU Quantum Center, University of the Basque Country UPV/EHU, Leioa, Biscay 48940, Spain

⁹ Department of Electrical Engineering, University of Southern California, Los Angeles, CA 90089, United States of America

¹⁰ Department of Chemistry, University of Southern California, Los Angeles, CA 90089, United States of America

This constitutes a beyond-breakeven fidelity improvement for DFS-encoded qubits. Our results showcase the potential utility of DFS codes as a pathway toward enhanced computational accuracy via logical encoding on quantum processors.

Keywords: quantum control, quantum error correction, quantum error suppression

1. Introduction

Scalable quantum computation relies on the ability to perform high-fidelity quantum logic operations. The path toward such operations is challenging due to inherent system-environment interactions and systematic errors. Ultimately, both induce noise processes that degrade qubit coherence and gate accuracy. Therefore, addressing noise in quantum systems is paramount to attaining viable and reliable quantum computation.

Broadly, approaches designed to manage noise in quantum systems seek to suppress, correct, or avoid errors [1]. Error suppression approaches (e.g. dynamical decoupling (DD) [2-4]) rely on the application of appropriately modulated control fields [5] such as fast and strong pulses to effectively average out noise [6]. In contrast, quantum error correction (QEC) leverages logical encodings of a collection of physical qubits to actively detect and correct errors [7–10]. As a passive alternative, decoherence-free subspaces (DFSs) and noiseless subsystems (NSs) form a special class of quantum codes that provide error avoidance by exploiting symmetries in the system-environment interaction [11–16]. The three approaches can be unified under a single, symmetry-based framework [17]. Error mitigation, the newest category of quantum error management, utilizes information from an ensemble of quantum experiments to reduce noise-biasing in expectation values [18]. While in principle, each class of protocols can be employed on its own, it has long been appreciated that practical quantum error management schemes are likely to necessitate multiple approaches working in concert [19–27] to achieve utility-scale quantum computation and, eventually, fault tolerance [28].

Despite the elusiveness of fault tolerance, utility-scale quantum computing may be on the horizon in part due to advancements in error management. Demonstrations on currently available noisy quantum processors have showcased the potential for classes of protocols to be executed independently and simultaneously. For example, confirmation of quantum error mitigation's effectiveness has been shown for quantum algorithms, such as the variational quantum eigensolver [29, 30] and quantum dynamics simulations [31]. Relatedly, a quantum algorithmic scaling advantage enabled by error suppression via DD has recently been demonstrated in superconducting systems [32, 33] building on longstanding experimental evidence of its utility [34–48]. Combining the two approaches has also been shown to be fruitful for enhancing quantum algorithm performance [31].

Noisy quantum devices have further led to proof-of-principle demonstrations of QEC [49–56]. This has included instances of error detection utilized to protect variational quantum algorithms [57]. Furthermore, verification of the added benefits of DD has been observed. For example, it has been incorporated into error correcting codes to protect idle qubits during long syndrome measurement acquisition and reset periods [52, 53, 56, 58, 59]. Error mitigation, DD, and quantum error detection have all been combined in a recent demonstration of better-than-classical execution of Grover's algorithm [60].

Despite early experimental instantiations [61–67], DFSs have yet to be examined as a scalable approach to error management in the current quantum computing era [68]. Their ability to circumvent measurement-based feedback gives them a potential advantage over their error-correcting counterparts. Furthermore, DFS codes can be readily integrated with error suppression to dynamically engineer the required symmetries of the code [21, 69–76]. Given their relative economy of qubit-and control-resource requirements, the question arises: what role can DFSs play in practical error management schemes for near-term and future quantum processors?

We address this question specifically for error-protected quantum memory and idle gates. DFSs are employed in conjunction with DD [77, 78] and error detection procedures to preserve logical qubit states on the IBM Quantum Platform (IBMQP) superconducting qubit processors. Specially designed DD sequences are used to engineer an effective noise environment and enforce symmetry conditions conducive to DFSs and NSs composed of two and three physical qubits, respectively. We present evidence for the existence of dynamically-generated DFSs and demonstrate their ability to surpass the fidelity of physical qubits subject to DD alone. The scalability of DFSs is showcased through the simultaneous generation and preservation of multiple independent logical qubits, where logical qubit fidelity up to 23% better than those achieved by the physical qubit constituents is observed. Together, these results highlight the potential utility of DFSs when used in conjunction with error suppression and detection procedures to enhance logical error management on quantum processors.

An overview of our methodology is presented in figure 1. Physical and logical protocols are compared by first encoding the qubits and then subjecting them to an error management protocol. As the objective is to evaluate each protocol's ability to preserve qubit states, we apply repetitions of said

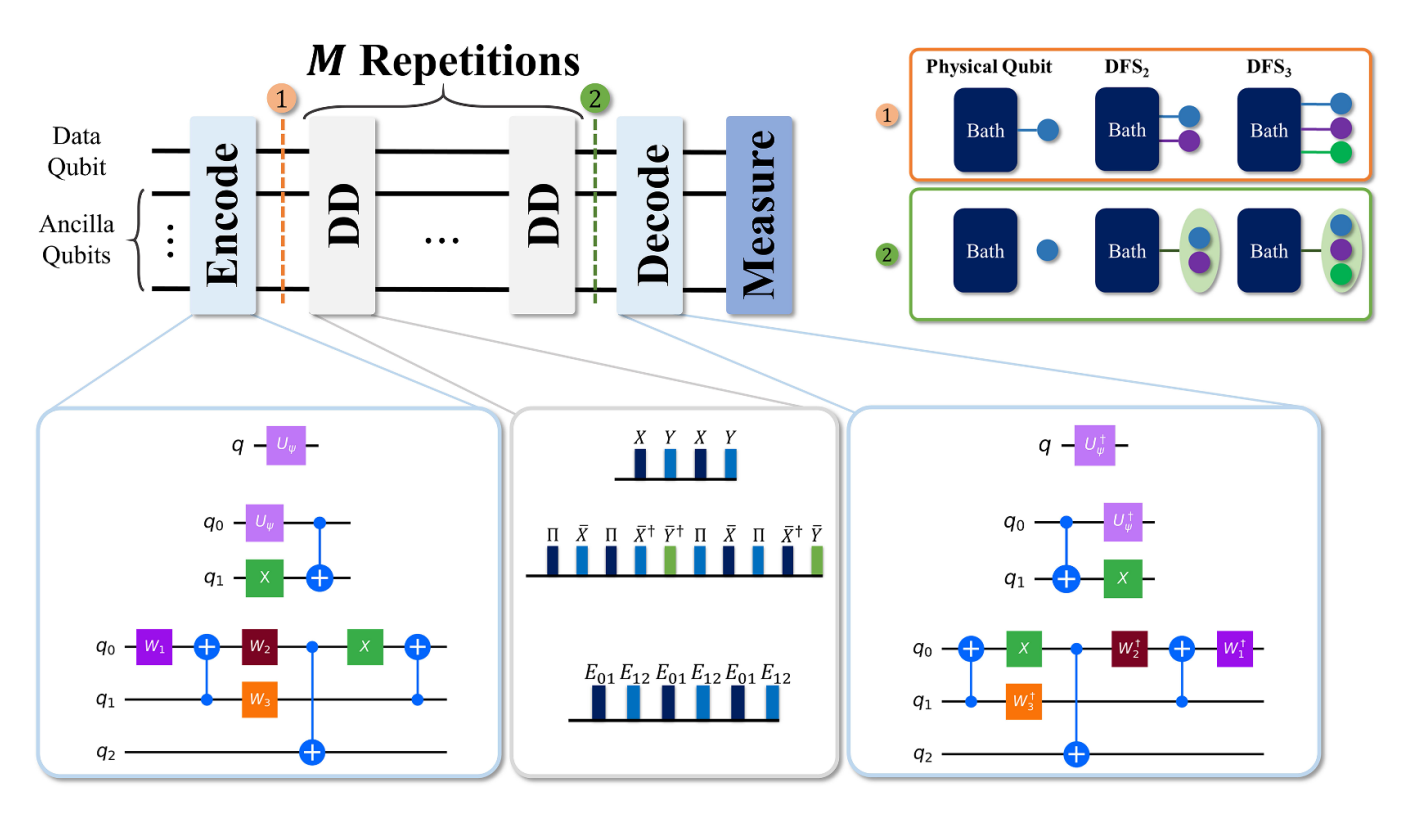


Figure 1. Schematic of the quantum state preservation experiment for all encoding schemes considered: unencoded (physical), 2-qubit DFS (DFS₂), and 3-qubit DFS (DFS₃). The qubits are initially prepared according to the encoding scheme and then subjected to M repetitions of DD or the equivalent free evolution duration, where the system is allowed to evolve according to its internal dynamics. The inverse of the encoding procedure is then used to decode the qubit states prior to measuring in the computational basis. The encoding step for the DFS₂ code utilizes the unitary U_{ψ} to prepare the desired single-qubit state $|\psi\rangle$ for the data qubit. In the 3-qubit encoding, W_j , j=1,2,3 are unitaries dependent upon the specifications of $|\psi\rangle$. Each encoding scheme is associated with a specific DD protocol. Unencoded evolution utilizes the XY4 universal decoupling sequence, while the 2-qubit DFS symmetrization sequence is composed of logical rotations about the x and y-axes of the logical qubit Bloch sphere. Noise symmetrization is achieved in the 3-qubit case using a sequence of SWAP operators E_{ij} . The upper-right panel provides an illustration of (1) the system-environment interaction prior to DD and (2) the desired interaction after DD. For physical qubits, the desired effect is a decoupling from the environment, while the DFS DD sequences seek to engineer a collective interaction with the environment. Further information regarding the encoding circuits and DD sequences can be found in the appendices appendices A–D.

protocols for equivalent time durations. State fidelity is then determined by applying a decoding operation and measuring in the computational basis. Physical qubits are protected by error suppression, while logical DFS qubits undergo error suppression and detection. We focus on the 2 and 3-qubit DFS code, with encoding operations and dynamical symmetry-generating sequences for each shown in the bottom-left and bottom-middle of figure 1, respectively. Error detection is applied after measurement via post-selection based on the state of the ancilla qubits. In addition to the subsequent sections, additional information regarding the state preparation circuits and DD sequences can be found in appendices appendices A–D.

This paper is organized as follows. In section 2, background on DFS codes and DD is presented. Sections 3 and 4 showcase the results of the study. Evidence of collective interactions generated by logical DD is exhibited in section 3, while time-dependent preservation is the focus of section 4. In the latter, we assess the performance of logical encodings against physical error suppression and highlight instances where DFS codes prevail. Section 5 summarizes the results and conclusions.

2. Decoherence-free subspaces and dynamical decoupling

2.1. Decoherence-free subspaces and noiseless subsystems

As passive error-correcting codes, DFSs leverage intrinsic symmetries in the system-environment interaction. Their construction is based on identifying subspaces of the system Hilbert space unaffected by noise. More concretely, consider an open quantum system described by the Hamiltonian

$$H = H_{\rm S} + H_{\rm B} + H_{\rm SB},\tag{1}$$

where $H_{\rm S}$ is the pure system Hamiltonian and $H_{\rm B}$ is the pure bath Hamiltonian, generating dynamics only within the system and bath Hilbert spaces $\mathcal{H}_{\rm S}$ and $\mathcal{H}_{\rm B}$, respectively. The interaction between the system and its environment is captured by $H_{\rm SB}$, which can be generically expressed as $H_{\rm SB} = \sum_{\alpha} A_{\alpha} \otimes B_{\alpha}$, where $\{A_{\alpha}\}$ and $\{B_{\alpha}\}$ act exclusively on the system and bath, respectively.

DFS encoding relies on finding a 'good' subspace $\mathcal{H}_G \subset \mathcal{H}_S$ that is unaffected by H_{SB} . As long as the system is initialized in \mathcal{H}_G and no operations are performed by H_S to take

the system out of \mathcal{H}_G , the time evolution will be unaffected by the decoherence resulting from H_{SB} [15]. Group theoretic arguments show that under reasonable mathematical assumptions about the system operators A_α , \mathcal{H}_G always exists and it is possible to perform scalable, universal quantum computation in the DFS [79]. More precisely, the system Hilbert space can be decomposed as a direct sum over the irreducible representations (irreps) J of the associative algebra \mathcal{A} generated by the set $\{A_\alpha\}$: $\mathcal{H}_S = \bigoplus_J \mathbb{C}^{n_J} \otimes \mathbb{C}^{d_J}$, such that each noiseless subsystem \mathbb{C}^{n_J} , where n_J is the degeneracy of irrep J, is invariant under the effects of \mathcal{A} [16]. That is,

$$A_{\alpha}|a\rangle\otimes|b\rangle=|a\rangle\otimes M_{\alpha}|b\rangle\quad\forall\alpha,\tag{2}$$

where the states $|a\rangle \in \mathbb{C}^{n_J}$ remain invariant under the error algebra \mathcal{A} , while $|b\rangle \in \mathbb{C}^{d_J}$ can be altered by the arbitrary operator M_α without consequence to the computation. Quantum information is stored in \mathbb{C}^{n_J} . When the irrep dimension $d_J=1$, $\mathbb{C}^{n_J} \otimes \mathbb{C}^{d_J}$ reduces to a DFS, i.e. a 'good' subspace $\mathcal{H}_G = \mathbb{C}^{n_J}$.

In this study, we employ DFS protection against collective interactions, which arises when the system-bath coupling is invariant under qubit permutation. The *N*-qubit system-environment interaction under such permutation symmetry is fully described in terms of the total spin operator $A_{\alpha} = \sum_{i=1}^{N} \sigma_{i}^{\alpha}$, where $\alpha \in \{+,-,z\}$; thus, $H_{\text{SB}}^{\text{col}} = \sum_{\alpha \in \{+,-,z\}} A_{\alpha} \otimes B_{\alpha}$. Below, DFS codes consisting of *N* qubits will be denoted as DFS_N for brevity.

2.1.1. Collective Dephasing DFS. The simplest type of collective system-bath interaction for which a DFS can be identified is collective dephasing, i.e., $H_{\rm SB}^{\rm col}$ with $B_{\pm} \equiv 0$. In turn, one can identify the smallest logical qubit encoded within two physical qubits. The subspace invariant under collective dephasing, which we refer to as DFS₂, is spanned by the logical states $|0_L\rangle = |01\rangle$ and $|1_L\rangle = |10\rangle$. Such states can be readily realized in semiconductor qubit systems [80–82] and have been demonstrated in other systems as well [61, 66, 83].

A circuit describing the generation of an arbitrary state $|\psi\rangle$ within the logical subspace is shown in figure 1. Logical manipulations that preserve the DFS consist of all Hermitian operators that belong to the commutant of the error algebra, $\mathcal{A}_z \equiv \{O: [O,A_z]=0\}$, i.e. all operators O that commute with the noise. One such set of encoding operators is given by

$$\bar{\sigma}^x = \frac{1}{2} \left(\sigma_1^x \sigma_2^x + \sigma_1^y \sigma_2^y \right) \tag{3a}$$

$$\bar{\sigma}^{y} = \frac{1}{2} \left(\sigma_{1}^{y} \sigma_{2}^{x} - \sigma_{1}^{x} \sigma_{2}^{y} \right), \tag{3b}$$

where $\bar{\sigma}^z = i[\bar{\sigma}^x, \bar{\sigma}^y]/2$ [79, 83]. Logical single-qubit rotations within the DFS are therefore defined by $\bar{R}_{\hat{n}}(\theta) = \exp(-i\theta\hat{n}\cdot\vec{\sigma})$, where $\vec{\sigma} = (\bar{\sigma}^x, \bar{\sigma}^y, \bar{\sigma}^z)$. Two qubit operations can be generated via a logical controlled phase gate of the form $\bar{R}^{ij}_{zz}(\theta) = \exp(-i\theta\bar{\sigma}^z_i\bar{\sigma}^z_j)$ [83, 84]. Alternatively, one can generate a logical CNOT between the *i*th and *j*th logical qubit using $\overline{\text{CNOT}}_{ij} = \text{CNOT}_{i_2\,j_1}\text{CNOT}_{i_2\,j_2}$. $\overline{\text{CNOT}}_{i_k\,j_l}$ defines the control (target) qubit as the *k*th (*l*th) physical qubit of the *i*th (*j*th) logical qubit.

2.1.2. Collective decoherence DFS. Decoherence-free subsystems, or NSs, build upon the notion of noise-invariant subspaces to more generally define subsystems corresponding to preserved degrees of freedom. Such a subsystem can be constructed when a quantum system is subject to collective decoherence, i.e. $B_z \neq 0$ and $B_{\pm} \neq 0$, using a minimum of three physical qubits [16, 85]. The logical space is constructed from four orthonormal states:

$$|\bar{1}\rangle = |S_0\rangle|0\rangle, \quad |\bar{2}\rangle = |S_0\rangle|1\rangle$$

$$|\bar{3}\rangle = \left(\sqrt{2}|T_+\rangle|1\rangle - |T_0\rangle|0\rangle\right)/\sqrt{3}$$

$$|\bar{4}\rangle = \left(|T_0\rangle|1\rangle - \sqrt{2}|T_-\rangle|0\rangle\right)/\sqrt{3}.$$
(4)

These states are composed of the singlet state $|S_0\rangle = (|01\rangle - |10\rangle)/\sqrt{2}$ and triplet states $|T_+\rangle = |00\rangle$, $|T_0\rangle = (|01\rangle + |10\rangle)/\sqrt{2}$, and $|T_-\rangle = |11\rangle$. While notably amenable to semiconductor qubit systems [82, 86], such states have been realized in nuclear magnetic resonance as well [62, 65].

The 3-qubit code (DFS₃) is defined by the logical states

$$|0_L\rangle = \gamma |\bar{1}\rangle + \delta |\bar{2}\rangle |1_L\rangle = \gamma |\bar{3}\rangle + \delta |\bar{4}\rangle,$$
(5)

where γ and δ specify the gauge. Note that here the gauge degrees of freedom are that of a single qubit and thus, $d_J = 2$. Figure 1 displays the encoding circuit for the DFS₃ code with $\gamma = 1$ and $\delta = 0$; see appendix A for an extension to arbitrary γ and δ . Computations on the three-qubit code are generated by the logical operators [79]:

$$\bar{\sigma}^x = \frac{1}{\sqrt{3}} \left(E_{23} - E_{13} \right) \tag{6}$$

$$\bar{\sigma}^z = \frac{1}{3} (E_{13} + E_{23} - 2E_{12}),$$
 (7)

where E_{ij} denotes a SWAP operation between the *i*th and *j*th physical qubits. We note as an aside, that this forms the basis for universal quantum computation using just the Heisenberg interaction [79, 87, 88], specifically in quantum dot systems [76, 86, 89].

2.2. Error detection in DFS codes

Passive quantum codes share many commonalities with their active correcting counterparts. Specifically, DFSs can be described as a highly degenerate quantum error correcting code with infinite distance when *all* operations are restricted to the code space. Of course, in practice, logical operations are not ideal and leakage outside of the code space can occur. It is in this domain that the stabilizer properties of the DFS codes can be employed for an additional layer of protection.

Under the stabilizer formalism, continuous (non-Abelian) stabilizers can be defined based on the DFS condition, equation (2) [79]. Collective dephasing yields $Z_{\text{col}} = \bigotimes_{i=1}^{N} Z_i$ as one of the stabilizer elements, while collective decoherence includes additional collective Pauli operations as stabilizer elements: $X_{\text{col}} = \bigotimes_{i=1}^{N} X_i$ and $Y_{\text{col}} = \bigotimes_{i=1}^{N} Y_i$. As a result, the

DFS can detect any odd number < N of single-qubit bit-flips under collective dephasing or of arbitrary single-qubit Pauli errors under collective decoherence.

We draw on the error detection properties of the code and complement the DFS and DD protocols with a post-selection (PS) procedure. In this way, we utilize the deferred measurement principle [90] to circumvent the need for costly midcircuit measurement and the introduction of additional ancilla qubits. Through the examination of the state probability distributions after decode and measurement, we define detectable error states specific to the code. Characteristics of these states are then used to define criteria for conditioning the state of the data qubit based on the state of ancilla qubits. In the case of the DFS₂, PS affords detection of single-qubit bit-flip errors. Similarly, for the DFS₃ code, PS can supply detection of bit-flip or phase-flip errors. We further elaborate on our procedures in appendix E.

2.3. Dynamically generated DFSs

2.3.1. Dynamical decoupling. Quantum processors rarely possess intrinsic noise environments with the ideal permutation symmetry of collective interactions. However, through the use of DD, such symmetries can be effectively engineered. DD sequences generally comprise control pulses applied at predetermined time intervals to modify the system-environment interaction $H_{\rm SB}$. Given a unitary evolution subject to the total Hamiltonian H (equation (1)),

$$f_{\tau} \equiv e^{-iH\tau},\tag{8}$$

DD sequences with delta-function-like pulses result in the evolution

$$U_{\rm DD}(T) = P_K f_{\tau} P_{K-1} f_{\tau} \dots P_1 f_{\tau}.$$

The total evolution time $T = K\tau$ and $\{P_j\}$ are the control pulses. Conventionally, DD sequences are designed to effectively cancel the system-bath interaction (i.e. $H_{\rm SB} = 0$) up to a certain order in T. More precisely, an ℓ th order decoupling sequence yields an effective time evolution given by $U_{\rm DD}(T) = e^{-i(H_{\rm S} + H_{\rm B})T} + \mathcal{O}[(\lambda T)^{\ell+1}]$, where λ depends on both $\|H_{\rm SB}\|$ and $\|H_{\rm B}\|$ [26, 91]. A notable example, which will be relevant in this study, is the universal decoupling sequence [3]

$$XY_4 = Yf_{\tau}Xf_{\tau}Yf_{\tau}Xf_{\tau}. \tag{9}$$

Utilizing X and Y pulses, representing π -rotations about the x and y axes of the single qubit Bloch sphere, respectively, XY_4 offers first order ($\ell=1$) decoupling for general single qubit noise.

Beyond suppression of system-environment interactions, DD can be used to selectively average out components of H_{SB} to create the necessary conditions for a DFS. The group-theoretic foundations for such 'symmetrizing' sequences are given in [4, 21]. Specific sequences for generating collective interactions are derived in [69] and are elaborated upon below. In principle, achieving symmetrization conditions conducive

to a DFS can require fewer pulses than complete suppression of general multi-qubit system-environment interactions [84]; this is a potential advantage of combining DFSs with DD.

2.3.2. Dynamically generated collective dephasing. Two-qubit collective dephasing is generated by DD sequences consisting of logical operations. In the most general two-qubit setting, where single and two-qubit couplings to the environment are allowed, two-qubit collective dephasing is created by a concatenation of three sequences consisting of rotations on the logical Bloch sphere (see appendix B):

$$\bar{Y} \circ \bar{X} \circ \Pi \circ f_{\tau} = \bar{Y}\bar{X}^{\dagger} f_{\tau} \Pi f_{\tau} \bar{X} f_{\tau} \Pi f_{\tau} \bar{Y}^{\dagger} \bar{X}^{\dagger} f_{\tau} \Pi f_{\tau} \bar{X} f_{\tau} \Pi f_{\tau}. \quad (10)$$

The inner-most sequence composed of $\Pi = \bar{R}_x(\pi)$ operations is used to suppress leakage out of the DFS. In contrast, concatenating logical operators $\bar{Y} = \bar{R}_y(\pi/2)$ and $\bar{X} = \bar{R}_x(\pi/2)$ enables cancellation of all logical single-qubit errors. Note that the suppression properties of the sequence are independent of concatenation ordering. All variations lead to an effective Hamiltonian $H_{\rm SB}^{\rm col}$ with $B_{\pm} \equiv 0$.

2.3.3. Dynamically generated collective decoherence. The three-qubit collective decoherence condition can be generated using the sequence

$$E_{12}f_{\tau}E_{01}f_{\tau}E_{12}f_{\tau}E_{01}f_{\tau}E_{12}f_{\tau}E_{01}f_{\tau}. \tag{11}$$

Intuitively, the resulting evolution is akin to rapidly swapping the states of the qubits such that the environment cannot distinguish between them [76, 92]. The sequence assumes the underlying noise model is given by $H_{\rm SB} = \sum_{j=1}^N \vec{\sigma}_j \cdot \vec{B}_j$, with $\vec{\sigma}_j = (\sigma_j^+, \sigma_j^-, \sigma_j^z)$ and $\vec{B}_j = (B_j^+, B_j^-, B_j^z)$. The effective Hamiltonian resulting from the DD sequence is $H_{\rm SB}^{\rm col}$.

Practical implementation of the above sequences on the IBMQP requires composite pulses consisting of multiple noisy two-qubit gates. For example, E_{jk} includes three CNOTs, each of which demands two faulty cross-resonance gates [93]; see appendix \mathbb{C} for further details. As such, realizations of these sequences are quite far from the noiseless, delta-function-pulse idealization from which they were derived. Nonetheless, as we show below, dynamically generating DFSs with these composite operations is achievable despite the imperfections inherent in the two-qubit gates.

3. Evidence of collective symmetry

3.1. Logical state invariance

We investigate the presence of native and dynamically generated collective decoherence on the IBMQP. A single logical qubit is compared against its physical qubit constituents using a state-dependent fidelity analysis. The system is prepared in a quantum state lying in the (x, z)-plane of the Bloch sphere, such that $|\psi(\theta)\rangle = \cos\left(\frac{\theta}{2}\right)|0\rangle + \sin\left(\frac{\theta}{2}\right)|1\rangle$ for physical qubits and equivalently $|\psi_L(\theta)\rangle = \cos\left(\frac{\theta}{2}\right)|0_L\rangle +$

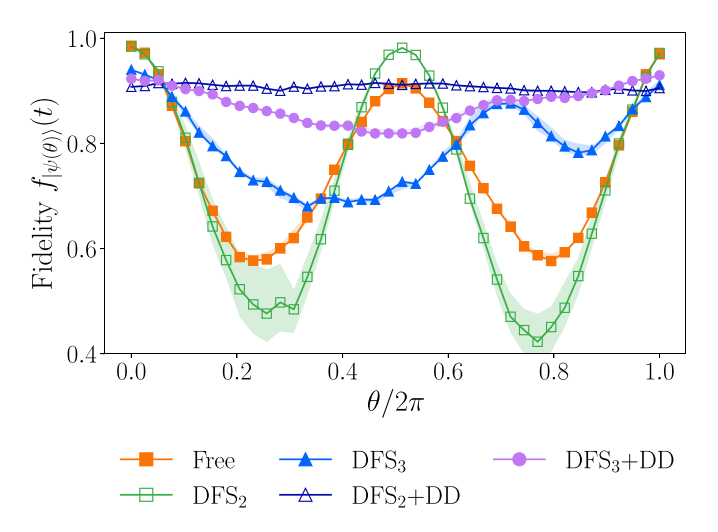


Figure 2. Fidelity as a function of elevation angle θ for unprotected and protected states. Initial states $|\psi(\theta)\rangle$ are chosen to be a subset of states that lie in the (x, z)-plane of the Bloch sphere. Each data point corresponds to the evolution of an unprotected or protected state for $T=14.89\mu s$, or the equivalent of M=1 repetitions of the DFS₂+DD sequence (M=2 repetitions of the DFS₃+DD sequence) with state encoding and decoding. DFS protocols (with post-selection) correspond to free evolution bookended by encoding and decoding circuits. State invariance is not observed, indicating that the native noise does not satisfy the DFS conditions. DFS₂+DD and DFS₃+DD utilize the collective symmetrizing DD and post-selection to achieve the expected state invariance (independence on θ). Data points represent estimated means and shaded regions denote 95% CIs, all of which are determined from bootstrapping over five realizations of the experiment. All data were collected from the five-qubit Manila device.

 $\sin\left(\frac{\theta}{2}\right)|1_L\rangle$ is defined for DFS codes. For the DFS₃ code (equation (5)), we first focus on the particular gauge $\gamma=1$ and $\delta=0$ for this comparison. An investigation of gauge dependence is presented below. We do not scan over the azimuthal angle ϕ as previous work has shown that the free evolution fidelity depends almost entirely on the elevation angle θ [43, 47] (see the discussion following equation (15) in [94] for an explanation of this effect).

Following physical or encoded state preparation, the system is allowed to freely evolve or is subjected to DD; the resulting state is denoted by $\rho_{\text{out}}(t)$. An inverse state preparation completes the evolution prior to measurement in the computational basis. This sequence of operations is used to evaluate a physical or logical protocol's ability to preserve an initial state via the state fidelity

$$f_{|\psi(\theta)\rangle}(t) = \langle \psi(\theta) | \rho_{\text{out}}(t) | \psi(\theta) \rangle,$$
 (12)

where $\rho_{\rm out}^{\rm ideal}(t) \equiv |\psi(\theta)\rangle\langle\psi(\theta)|$. We investigate this fidelity as a function of θ for both unprotected states undergoing free evolution and protected states. The term 'protected' refers to both DD and logical DFS encodings, or their combination.

Unprotected states are obtained from idle (free) evolution, where the system is allowed to evolve according to its internal dynamics after state preparation. In order to equalize qubit resources between unprotected and encoded states, we report the best fidelity of three adjacent physical qubits. Unprotected states are compared against DFS encodings without DD (DFS₂, DFS₃) and with DD (DFS₂+DD, DFS₃+DD). All results, unless otherwise specified, include PS. For the DFS₂ code, PS is performed by conditioning the data qubit state on the ancilla returning to the ground state. Alternatively, the

DFS₃ code utilizes a PS procedure that is based on conditioning the data qubit state on qubit q_2 (see figure 1) returning to the ground state. We find that PS leads to an overall increase in fidelity for both logical encodings whether or not DD is employed. This is discussed further in section 4.1, with additional details presented in appendices E and I.

In figure 2, we show the state fidelity $f_{|\psi(\theta)\rangle}(t)$ as a function of θ for a total evolution time of $t\approx 14.89\,\mu s$, or one repetition of the DFS₂+DD sequence (two repetitions of the DFS₃+DD sequence), including logical state encoding/decoding. Experiments are performed on the five-qubit Manila device using qubits (2, 3, 4); see appendix F for further details regarding device specifications. While this subset of qubits yields the highest fidelity for logical encodings, we observe qualitatively similar behavior for alternative configurations; see appendix J. Estimates of fidelity (solid lines) and 95% confidence intervals (CIs; shaded regions) are determined by bootstrapping over five realizations of the demonstration using 8000 measurement shots.

Logical encodings alone are not sufficient to observe collective dephasing/decoherence. The DFS₂ code exhibits a state-dependent fidelity that is more consistent with free evolution than collective dephasing. In particular, we observe substantial degradation in fidelity for states close to the (x, y)-plane of the logical qubit Bloch sphere. In this regime, logical states are most susceptible to phase errors, which may arise from coherent (i.e. detuning or crosstalk) or dissipative (i.e. phase damping) noise. Importantly, these noise sources are not typically uniform across qubits on the IBMQP [46, 95, 96] and thus, are not invariant under the DFS₂ code. Similarly, non-uniform phase errors contribute to the logical state dependence observed for the DFS₃ code. As we show via

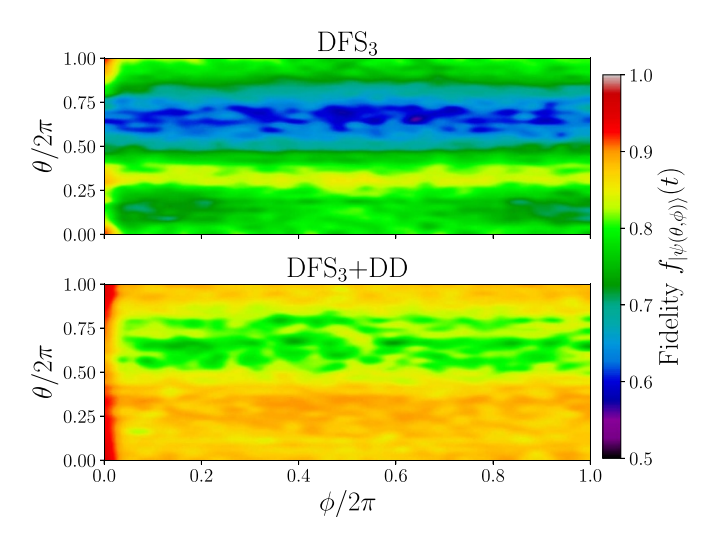


Figure 3. Investigation of gauge invariance for the DFS₃ code. State fidelity as a function of initial state $|\psi(\theta,\phi)\rangle$ is plotted for the DFS₃ (top) and DFS₃+DD (bottom) protocols. In the former, the system is encoded in the DFS₃ code, subject to free evolution equivalent to M=1 repetitions of the DFS₃ DD sequence, and returned to the ground state prior to measurement. The latter follows a similar procedure, except the free evolution is replaced by the symmetrizing DD sequence. Both protocols include PS. Plots show mean fidelities estimated from bootstrapping data collected over a five-day period on Manila; 8000 measurement shots are used. Results indicate an enhanced gauge invariance when using the DFS₃ encoding in conjunction with PS and DD.

simulation in appendix H, non-uniform phase errors can lead to an asymmetric θ -dependence in the fidelity.

The inclusion of DD leads to substantially different behavior. Phase errors are symmetrized and thus, the DFS₂+DD protocol produces a near-state-invariant behavior consistent with collective dephasing. DD is beneficial for nearly all states considered, except for those near $\theta=0$. This result is consistent with previous studies of DD on physical qubits [43]. Namely, faulty DD pulses can lead to a combined error accumulation that is greater than allowing the qubits to idle. In the case of the DFS₂ code, $f_{|\psi(0)\rangle}(t) = 0.984$ without DD (similar to the free evolution case: $f_{|\psi(0)\rangle}(t) = 0.986$), while with DD $f_{|\psi(0)\rangle}(t) = 0.908$. The DFS₃ code does not display such a significant difference $(f_{|\psi(0)\rangle}(t) = 0.923$ and $f_{|\psi(0)\rangle}(t) = 0.94$ for the code with and without DD, respectively) most likely due to the large depth state preparation circuit which may induce a majority of the error.

Similar to the two-qubit code, the DFS₃+DD protocol conveys enhanced state invariance. Residual θ -dependence remains, however, specifically for states near $\theta=\pi$. Analyzing the measurement outcome distributions for $\theta<\pi/2$, we find that a majority of the errors are consistent with phase errors. The PS procedure assists in discarding a substantial subset of these errors, primarily leaving less probable single-qubit bit-flip errors. For $\pi/2 \le \theta \le \pi$, we observe an increase in bit-flip errors. As a result, the PS procedure partially biases state fidelities such that smaller elevation angles yield higher fidelity. We further elaborate on the effect of PS in appendix I.1.

3.2. Gauge invariance

Noiseless subsystems possess a gauge invariance that enables the logical computational basis states to be defined as subsystems, rather than subspaces. As an additional verification of collective decoherence generation, we examine the existence of this gauge invariance for the DFS $_3$ code. We perform a state-dependent analysis similar to the previous subsection but also permit rotations within the gauge subspace. More concretely, we consider states of the form

$$|\psi(\theta,\phi)\rangle = \cos\left(\frac{\theta}{2}\right)|0_L(\phi)\rangle + \sin\left(\frac{\theta}{2}\right)|1_L(\phi)\rangle,$$
 (13)

where

$$|0_{L}(\phi)\rangle = \cos(\phi/2)|\bar{1}\rangle + \sin(\phi/2)|\bar{2}\rangle |1_{L}(\phi)\rangle = \cos(\phi/2)|\bar{3}\rangle + \sin(\phi/2)|\bar{4}\rangle,$$
(14)

with the four constituent states defined in equation (4). The DFS₃ code is prepared via the above state and subject to a single repetition of the DFS₃+DD sequence or allowed to freely evolve for an equivalent duration. The state decoding procedure is performed before measurement in the computational basis and subsequent PS.

A comparison between a freely evolving DFS₃ and the DFS₃+DD protocol is shown in figure 3. Experiments are performed on the five-qubit Manila device using 8000 measurement shots. Estimates of mean fidelity (equation (12)) are determined by bootstrapping over five realizations of the demonstration.

Evidence of gauge invariance is observed for both the DFS₃ encoding alone and with the inclusion of the collective-symmetry-generating DD protocol. In the top panel of figure 3, the DFS₃ fidelity determined via equation (12) is shown as a function of θ and ϕ . While there is a clear dependence of fidelity on the logical state, signatures of invariance to the gauge are more prominent. We quantify this invariance by examining the standard deviation of the fidelity over the gauge states and averaged over initial logical states. For the DFS₃ encoding, the average standard deviation in fidelity is 0.023. In contrast, the

DFS₃+DD protocol exhibits an average standard deviation of 0.018. The absence of a significant difference in gauge invariance between the DFS₃ and DFS₃+DD protocols indicates that the gauge degree of freedom is robust under this device's intrinsic decoherence mechanisms.

Consistent with the analysis in the previous subsection, DD improves the fidelity for all NS logical states. One of the most prominent features is the significant boost in fidelity for the gauge state with $\phi=0$; see the bottom panel of figure 3. This feature is easily explained by the state preparation circuit which requires an additional CNOT gate between the ancilla qubits for all $\phi\neq0$. Ultimately, due to the topology of the hardware, this requires an additional SWAP operation as well; hence, the notable degradation in fidelity. Further details regarding the $\phi\neq0$ state preparation are discussed in appendix A.

4. Preservation of logical qubits

Ultimately, the goal of our protection protocols is to extend the preservation of arbitrary quantum states. In this section, we evaluate each protocol's performance by allowing the system to evolve under free or controlled evolution, i.e. the experiment depicted schematically in figure 1. Under unprotected (free) evolution, we prepare the state $U|0\rangle$ (we define U below), let the system evolve according to its internal dynamics for fixed periods of time, apply U^{\dagger} , and measure in the computational basis. In the protected case, after encoding followed by the application of \bar{U} (logical-U), the system is subject to M repetitions of a DD sequence for a total evolution time of $T_{\rm DD}(M) = Mt_{\rm DD}$, where $t_{\rm DD}$ is the time for a single DD cycle. As in the case of free evolution, the experiment is completed by applying \bar{U}^{\dagger} (decoding) and a measurement of all qubits in the computational basis. Below, we examine arbitrary state preservation for logical qubit encodings, starting with a single logical qubit and then scaling the protocols up to seven logical qubits. Unprotected states are compared against protected states using equivalent physical resources.

4.1. Preservation of one logical qubit

First, we focus on the time-dependent state preservation of a single logical DFS qubit. Ideally, the preservation of an arbitrary state would be determined by sampling over the Haar distribution and calculating the average fidelity $\mathbb{E}_{\text{Haar}}[f_{|\psi\rangle}(t)] = \int \mathrm{d}\psi f_{|\psi\rangle}(t)$ [90]. We estimate the Haar fidelity via

$$F(t) = \frac{1}{L} \sum_{i=1}^{L} f_{|\psi_i\rangle}(t), \qquad (15)$$

using an ensemble of L=20 states consisting of 14 Haar random states and the six eigenstates of the Pauli matrices, which we refer to as the poles of the Bloch sphere. We find this set to be sufficient for estimating $\mathbb{E}_{\text{Haar}}[f_{|\psi\rangle}(t)]$.

The average fidelity as a function of time is shown in figure 4 for experiments performed on the five-qubit Manila

device. Mean fidelities and error bars are determined by bootstrapping over five realizations of the experiment and 8000 measurement shots. As in section 3.1, results are shown for the configuration of qubits with the highest average fidelity for logical encodings, i.e. qubits (2, 3, 4). Results for physical qubits consider the highest average fidelity among the three physical qubits used for the DFS₃ code. While the DFS₂ code only requires two physical qubits, we do not find a significant difference in performance when selecting the best performing qubit among two or three physical qubits. This holds for both the Free and XY4 cases. In the latter, the best performing qubit is typically the one subject to DD; hence, an additional neighbor qubit evolving freely does not alter the best performance.

Solid lines designate fits to the data using

$$F(t) = C_1 f(t) + C_2,$$

$$f(t) = e^{-t/\tau_1} \cos(\omega t) + e^{-t/\tau_2}.$$
(16)

 C_1, C_2 denote dimensionless weight parameters, such that

$$C_1 = \frac{F(T_{\text{max}}) - F(T_0)}{f(T_{\text{max}}) - f(T_0)}, \quad C_2 = F(T_0) - C_1 f(T_0).$$
 (17)

The time required to evolve the system for $M_{\rm max}$ repetitions of a DD sequence (or the free evolution equivalent) is given by $T_{\rm max} = T_0 + T_{\rm DD}(M_{\rm max})$, where T_0 is the time for state encode, decode, and measurement. Short and long-term coherence times are determined by τ_1 and τ_2 , respectively, while ω is the oscillation frequency. Additional information regarding the fitting procedure can be found in appendix G.

Figure 4(a) displays the time-dependent state-averaged fidelity for unprotected physical (Free) and logical (DFS₂, DFS₃) qubits subject to PS alone. The fidelities of the Free and DFS₂ cases are statistically indistinguishable. However, the DFS₃ case has a notably longer short-term decay time, while its long-time decay is essentially infinite; see table 1. The longer decay time is accompanied by a higher fidelity. We attribute PS to the enhancement in fidelity, and substantiate this claim via an examination of the time-averaged fidelity:

$$\mathcal{F}_T = \frac{1}{T - T_0} \int_{T_0}^T F(t) \, \mathrm{d}t.$$
 (18)

In figure 4(c), the time-averaged fidelity is shown for all protocols in two regimes designated by the DD repetition time of the sequence used for the DFS₂ code. The short-time limit is set by the single repetition time $T = T_0 + t_{\rm DD} \approx 14.89 \,\mu{\rm s}$, where $T_0 \approx 0.81 \,\mu{\rm s}$, while the long-time limit corresponds to M = 3, i.e., $T = T_0 + 3 \,t_{\rm DD} \approx 43.05 \,\mu{\rm s}$. All estimates of \mathcal{F}_T are calculated by cubic spline integration, with subsequent means and CIs determined by bootstrapping.

The DFS₃ code benefits substantially from PS in both the short and long-time limit. PS results in approximately 14% and 17% improvement in the DFS₃ time-averaged fidelity over the bare encoding, respectively. The DFS₂ code obtains a mere 1.3% and 3% in comparison. This result is consistent with the stabilizer properties of the code in the sense that the DFS₂ code

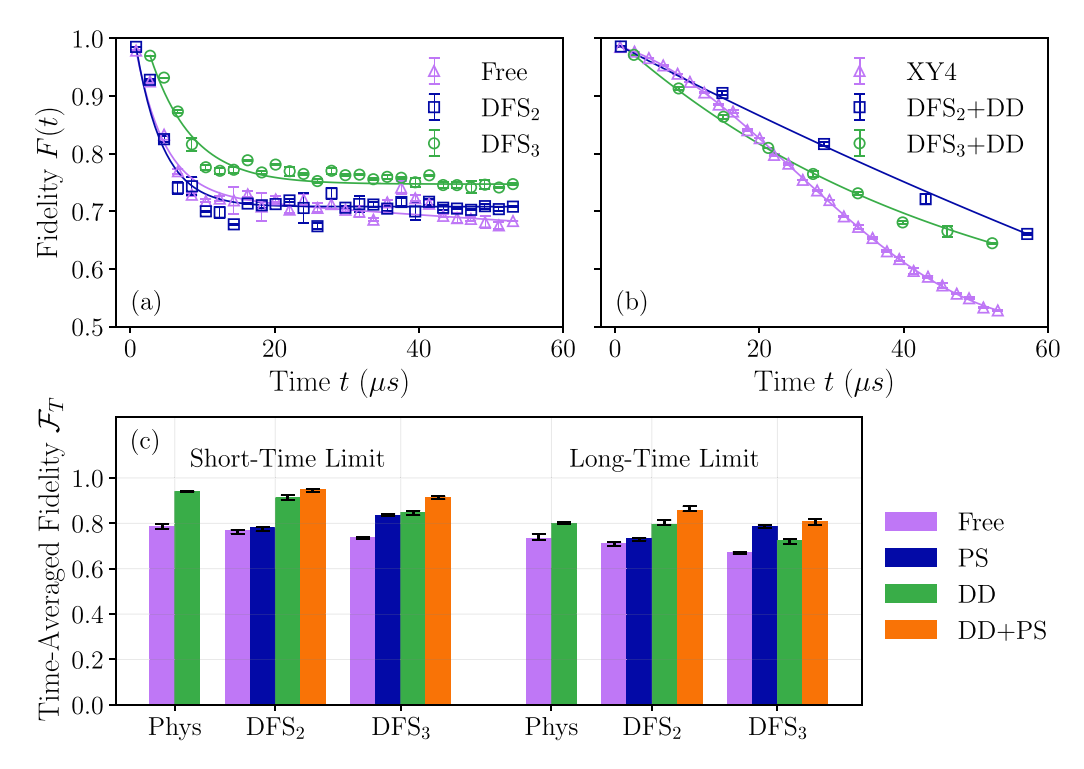


Figure 4. Time-dependent arbitrary state preservation of a single logical qubit. DFS encodings are compared against unencoded qubits using equivalent physical resources. Panel (a) shows the decay of logical states encoded within the DFS codes and subject to PS. The DFS₃ code appears to benefit the most from PS, achieving an improvement in performance over physical qubits subject to free evolution alone. In (b), logical encodings are used in conjunction with DD and PS and compared against XY4 on a physical qubit. Logical protocols outperform physical protocols particularly for M > 2 repetitions of logical DD. The behavior of each protocol is further captured by panel (c) in the short and long-time limit via the time-averaged fidelity (equation (18)). All experimental data is collected from the 5-qubit Manila device using 8000 measurement shots. Estimates of means and CIs are determined by bootstrapping five realizations of the data collected over five days.

Table 1. Fit parameters and standard error estimates for the fidelity decay of various logical and physical protocols. Corresponding fits are shown in figure 4, while the fit is given by equation (16).

Protocol	$\tau_1 (\mu s)$	ω (Hz)	$ au_2$ (μ s)	$F(T_0)$
Free	3.95 ± 0.55	0	319.98 ± 88.35	0.98 ± 0.02
XY4	100.49 ± 3.26	265.03	∞	0.99
DFS ₂ w/PS	3.79 ± 0.36	0	∞	0.99 ± 0.01
DFS ₂ w/DD+PS	229.91 ± 29.41	0	∞	0.99 ± 0.01
DFS ₃ w/PS	5.86 ± 0.42	0	∞	0.97 ± 0.01
DFS ₃ w/DD+PS	47.35 ± 3.94	0	∞	0.97

cannot detect all single-qubit errors and is limited to bit-flips. The DFS₃ possesses a larger set of detectable errors and therefore, obtains a more robust code space.

In examining the enhancement afforded by error detection as a function of the initial state, we find that the DFS₃ particularly benefits from PS for states approaching $\theta = 0$ on the logical Bloch sphere; see appendix I. States near the logical (x,y)-plane suffer from logical errors that typically render lower fidelities with PS. In contrast, DFS₂ logical states only gain from PS near the logical $|+\rangle$ state. Ultimately, this behavior leads to state-averaged fidelities that favor DFS₃ when error detection is employed.

Despite the utility of PS, DD typically results in greater improvement in fidelity. In the case of DFS₂, the short-time decay rate is greatly enhanced by the inclusion of DD. For example, we observed an approximate $60 \times$ increase in τ_1

(from 3.79 μ s to 229.91 μ s) when DD is used in conjunction with PS as compared to PS alone. Qualitatively similar behavior appears for the time-averaged fidelity as well. DD results in a short-time limit increase of 17% and long-time limit increase of 3% relative to PS. Further incorporating PS with DD boosts \mathcal{F}_T by 3% and 7%, respectively, indicating that (1) DD is most impactful in the short-time limit (consistent with DD's propensity to suppress non-Markovian but not Markovian errors) and (2) both protocols perform best when used together.

The DFS₃ code exhibits similar characteristics, however, PS plays an important role in the short-time limit as well. On their own, PS and DD enable similar short-time fidelities; DD yields a 15% increase over the DFS alone, with PS further improving the DFS₃+DD fidelity by 7%. This is accompanied by a nearly $8 \times$ improvement in τ_1 from 5.86 μ s for DFS₃

with PS to 47.35 μ s when DD is incorporated. In contrast, DD has a less appreciable effect on \mathcal{F}_T in the long-time limit. DD enhances the time-averaged fidelity of the DFS₃ code (without PS) by approximately 8%. DD and PS again prove to be more beneficial when used together, achieving a 21% increase over the DFS₃ encoding alone.

In figure 4(b), the logical encoding schemes with PS and DD are compared against DD on physical qubits. Qubit 3 is subject to XY4, while qubits 2 and 4 are allowed to evolve freely. After each total evolution time, the best qubit fidelity is taken, where the DD cycle time is $t_{\rm DD} = 4t_{\rm g} \approx 142.2$ ns for a gate time of $t_{\rm g} \approx 35.6$ ns. Alternative physical DD protocols were considered as well, e.g. applying XY4 simultaneously on all qubits, however, they typically resulted in worse fidelity. We attribute the degradation in fidelity to quantum crosstalk, which is exacerbated by simultaneous operations on nearestneighbor qubits. As such, the protocol chosen here is one such approach that suppresses parasitic interactions and combats local environmental noise.

Utilizing XY4 as a benchmark for noise protection in physical qubits, we evaluate each logical protocol's ability to outperform its physical qubit constituents. We find that DFS₂ (with DD and PS) and XY4 possess comparable short-time fidelity decay; see table 1. Similar results are observed for the time-averaged fidelity in the short-time limit. However, in the long-time limit, the distinction between the protocols becomes more apparent. The DFS₂ code with DD and PS achieves a 7.25% improvement over XY4, while the DFS₃ code attains a 1.25% enhancement. Overall, these results indicate that it is possible for DFS encodings to perform on-par with physical error suppression protocols in the short-time limit, while providing greater long-term protection of quantum memory.

4.2. Preservation of multiple logical qubits

In order to justify the resource overhead of logical encoding, one must demonstrate that K logical qubits can yield performance advantages over N = nK physical qubits, where n is the encoding overhead, i.e. n = 2 and 3 for the DFS₂ and DFS₃ cases, respectively. The analysis in the previous subsection sheds light on this comparison for K=1, where a single logical qubit performs similarly, if not better than physical qubits alone. We now expand this analysis to determine whether performance advantages persist with increasing K. We focus on the preservation of the best K physically adjacent logical (physical) qubits selected from a set of K' simultaneously generated logical (physical) qubits. Prepared in this way, the logical qubits are not readily amenable to twoqubit logical operations, as additional symmetrizing operations are required [69, 75]. However, this comparison provides key insight into a significant preliminary milestone: the simultaneous preservation of multiple independent logical qubits.

In figure 5, we summarize two comparisons in which N = 14 (N = 18) physical qubits are encoded into K' = 7 DFS₂ (K' = 6 DFS₃) logical qubits on the 27-qubit Montreal device.

(Device specifications are discussed in appendix F.) The time-averaged fidelity serves as the comparison metric, where T is the total time for encoding/decoding and one repetition of the DFS₂+DD sequence, i.e. the so-called 'short-time limit' discussed in section 4.1. The state-average fidelity is estimated for the L=20 states discussed in section 4.1, using 8000 measurement shots. \mathcal{F}_T is determined by cubic spline integration of F(t) up to $T\approx 26.65\,\mu s$. This is approximately equivalent to two repetitions of the DFS₃ DD sequence, including state encode/decode procedures. Estimates of the mean and CI for the time-averaged fidelity are determined by bootstrapping.

Logical qubits are compared against physical qubits using a combination of DD and free evolution. We consider physical qubit protocols corresponding to free evolution on all qubits and a DD-protection scheme in which every other qubit within the array is subject to XY4. Those qubits not protected by DD are allowed to evolve freely. As in the case of the single logical qubit, this protocol outperforms simultaneously XY4 on all qubits due to its suppression of parasitic crosstalk [46, 48]. A schematic illustration of the DD protocol is shown below panels (a) and (b) in figure 5. We consider similar logical encoding schemes: (1) the qubits are prepared in the logical subspace and allowed to evolve freely and (2) upon preparing the logical subspaces, every other logical qubit is subject to the symmetrizing DD sequence. As in the case of the physical qubit DDprotection protocol, we find that simultaneous logical operations on neighboring qubits typically result in lower fidelity. As before, we suspect this behavior is due to crosstalk between neighboring physical qubits that propagates into logical errors. The logical qubit DD-protection protocols for the DFS₂ and DFS₃ encodings are summarized at the bottom of figures 5(a) and (b), respectively.

Above the protocol schematics in figure 5 are comparisons of the time-averaged fidelity as a function of the number of logical qubits for each protocol. In panel (a), results are shown for the DFS₂ code. Among the available 27 qubits, we select the best set of N = 14 physically adjacent physical qubits based on CNOT gate error rates and decoherence times to perform our demonstrations. Physical qubit protocols are applied to the N-qubit set, while the DFS₂ protocols involve encoding the N qubits into K' = 7 logical qubits. We then ask the question: requiring physical adjacency, how do the best K logical qubits compare against the best K physical qubits? Panel (a) summarizes our findings as a function of K, where the DFS₂ encoding with PS typically performs similarly to physical qubit free evolution. In contrast, upon incorporating DD, the DFS₂ code outperforms the physical qubit DD protocol particularly for K > 2. Within error bars, the performance advantage of the DFS remains consistent up to K = 7, where time-averaged fidelities range from 12.5% to 24.7% higher than DD-protected physical qubits.

The performance advantage of DFS₃ over physical qubits is even more substantial than DFS₂. In figure 5(b), N = 18 qubits are again selected based on CNOT gate error rates and decoherence times. Physical qubit protocols on N qubits are compared against the DFS₃ protocols on K' = 6 logical qubits.

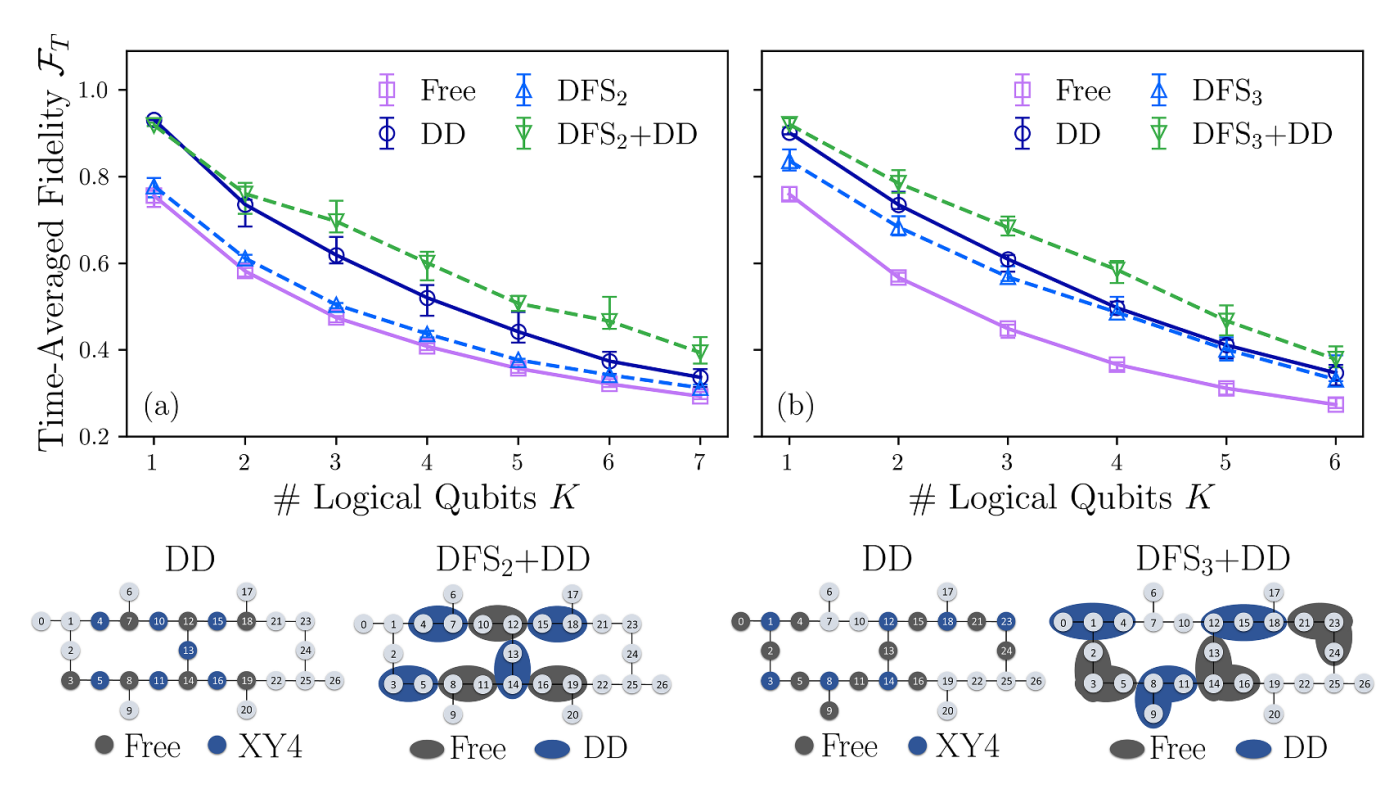


Figure 5. Time-averaged fidelity \mathcal{F}_T as a function of the number of logical qubits. Panels (a) and (b) show results comparing physical and logical protocols for the DFS₂ and DFS₃ encodings, respectively. The DD and DFS₂+DD protocol is shown below panel (a), while a similar illustration for the DFS₃ comparison is shown below panel (b). Each panel includes free-evolution (purple squares; solid line), physical qubit DD (dark-blue circles; solid line), the DFS_N (light blue up-triangles; dashed line), and DFS_N+DD (green down-triangles; dashed line) protocols. For the DFS₂ code, N=14 physical qubits are simultaneously prepared into K'=7 physically adjacent logical qubits. The time-averaged fidelity is examined for the best $K \le K'$ logical qubits using a total time of $T=26.65\,\mu s$, or one repetition of the longest DFS₂+DD sequence. An identical analysis is performed for the DFS₃ using N=18 physical qubits to prepare K'=6 logical qubits. Physical qubit fidelities are determined from the best K adjacent physical qubits among the available N. Experiments are performed on the 27-qubit Montreal device using 8000 measurement shots. Estimates of \mathcal{F}_T means and CIs are determined from bootstrapping five realizations of the data captured over five days. The results indicate that both the DFS₂+DD and DFS₃+DD protocols with PS outperform the physical DD protocol, particularly for K>2.

Contrary to the DFS₂ code, the DFS₃ code with PS alone yields sizable and consistent advantages over physical qubits subjected to free evolution; note the consistency with the discussion in section 4.1. We find that this performance advantage persists as the number of logical qubits increases. Surprisingly, the benefits of the DFS₃ with PS are considerable enough to result in near-equivalent time-averaged fidelity with that of DD on physical qubits, particularly for K > 3. As in the case of the DFS₂ encoding, the inclusion of DD results in improved fidelity for the DFS₃ code. The relative improvement in timeaveraged fidelity varies from approximately 9.7%-17.7% over the physical qubit DD protocol beyond K = 1. If instead the time-averaged fidelity is considered up to one cycle of the DFS₃ ($T \approx 12.33 \ \mu s$) then a maximum improvement of 23.6% over physical DD is achievable; a result comparable to the DFS₂ case. In both cases, we find that DFS encoding, when combined with error detection and suppression outperforms physical error suppression on its own.

5. Conclusions

In this work, we investigated the viability of DFS codes on currently available quantum devices. Using IBMQP superconducting qubit devices, we showed that DFS codes can achieve advantages over physical error suppression in the task of quantum state preservation. This was accomplished by devising logical qubit protection protocols that incorporate two key aspects: (1) noise-symmetrizing DD and (2) error detection provided by the stabilizer properties of the code. We established the advantage of these protocols for up to seven logical qubits, hence demonstrating their potential applicability and scalability on current and near-term quantum processors.

In evaluating the efficacy of the codes, we showed that the collective system-bath interactions required by DFS codes do not natively exist on the devices. However, such symmetries can be enforced through the application of specially designed pulse sequences. Despite their considerable gate depth, these

sequences enable logical subspace invariance indicative of a DFS code with fidelity gains relative to unencoded qubits.

We showed that state invariance leads to improved logical qubit fidelity over error suppression protocols that are applied directly to physical qubits. We observed an enhancement in fidelity up to seven DFS₂ and six DFS₃ qubits encoded into 14 and 18 physical qubits, respectively. Error detection employed via post-selection resulted in logical qubit fidelities that surpass the XY4 DD sequence, particularly in the case of the DFS₃ code. Moreover, when noise-symmetrizing DD was used in conjunction with post-selection, even greater performance gains were attainable. The DFS codes obtained up to a 24% and 17% improvement over XY4 in terms of the time-averaged fidelity, respectively. This constitutes a beyond-breakeven fidelity improvement for DFS-encoded qubits.

Additional studies are required to investigate the potential practical implementation of encoded quantum computation based on DFS codes. In particular, a demonstration of entangled logical qubits based on the methods we explored here is a natural next step. Nevertheless, we have already found encouraging results for the preservation of quantum states encoded within noninteracting copies of multiple logical qubits. Our protocol integrates error detection, avoidance, and suppression, and thus, highlights the significant potential of constructing error management schemes consisting of numerous techniques working in concert to enhance logical qubit fidelity.

Data availability statement

The data must be reviewed and released by the Johns Hopkins University Applied Physics Laboratory before being released. The distribution of the data is limited to domestic institutions only. The data that support the findings of this study are available upon reasonable request from the authors.

Acknowledgments

G Q thanks Colin Trout for insightful discussions. B P is grateful to Namit Anand and Haimeng Zhang for useful comments. This work was supported in part by the U.S. Department of Energy (DOE), Office of Science, Office of Advanced Scientific Computing Research (ASCR) Quantum Computing Application Teams program under fieldwork proposal number ERKJ34 and the Accelerated Research in Quantum Computing program under Award Number DE-SC0020316. This research was supported by the ARO MURI Grant W911NF-22-S-0007 and is based in part upon work supported by the National Science Foundation the Quantum Leap Big Idea under Grant No. OMA-1936388. This material is also based upon work supported by the Defense Advanced Research Projects Agency (DARPA) under Contract No. HR001122C0063. L A W

is supported by Grant No. PID2021-126273NB-I00 funded by MCIN/AEI/10.13039/501100011033, and the Basque Government through Grant No. IT1470-22. This research used resources of the Oak Ridge Leadership Computing Facility, which is a DOE Office of Science User Facility supported under Contract DE-AC05-00OR22725.

Appendix A. DFS₃ state preparation

The DFS₃ encoded states are prepared using the circuit defined in [97] and shown in figure 6. q0 denotes the data qubit, while q1 and q2 designate an additional ancilla qubit and gauge qubit, respectively. The controlled unitaries shown in the unoptimized circuit of figure 6(a) are defined via

$$G_1 = \frac{1}{\sqrt{3}} \begin{pmatrix} 1 & \sqrt{2} \\ -\sqrt{2} & 1 \end{pmatrix} \tag{A1}$$

$$G_2 = \frac{1}{\sqrt{2}} \begin{pmatrix} 1 & 1 \\ -1 & 1 \end{pmatrix}. \tag{A2}$$

The circuit defined within the gray, dashed box is only executed if the gauge qubit is prepared in any state other than $|0\rangle$. Note that by definition of the DFS₃ code, the gauge qubit can be initialized in any state while still satisfying the DFS preservation condition.

Compiling the state preparation circuit to the IBMQP gateset requires decomposition of the controlled gates CG_1 and CG_2 . The combined product of these gates can be replaced by a circuit that only requires one CNOT gate. This decomposition is accomplished via the Schmidt decomposition, where $|\Psi\rangle = CG_2CG_1|\psi\rangle\otimes|0\rangle$ is rewritten as

$$|\Psi\rangle = \alpha |\psi_1\rangle \otimes |\phi_1\rangle + \beta |\psi_2\rangle \otimes |\phi_2\rangle,$$
 (A3)

where $\langle \psi_1 | \psi_2 \rangle = \langle \phi_1 | \phi_2 \rangle = 0$. The Schmidt decomposition is computed by taking the partial trace of each of the bipartite systems and computing the corresponding eigenvalues. For $\rho_{AB} = |\Psi\rangle\langle\Psi|$, we have $\rho_A = \mathrm{Tr}_B[\rho_{AB}]$ and $\rho_B = \mathrm{Tr}_A[\rho_{AB}]$. We denote by α, β the eigenvalues of ρ_A . The eigenstates of ρ_A and ρ_B are $|\psi_i\rangle$ and $|\phi_i\rangle$, respectively. The resulting unitaries from the decomposition are:

$$\tilde{W}_{1} = \begin{pmatrix} \alpha & \beta^{*} \\ \beta & -\alpha^{*} \end{pmatrix}, \tag{A4}$$

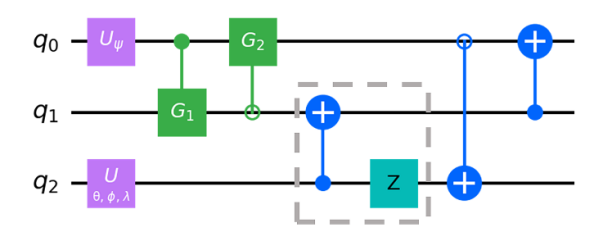
which can be derived from the Schmidt eigenvalues, and

$$W_2 = |\psi_1\rangle\langle 0| + |\psi_2\rangle\langle 1|,$$

$$W_3 = |\phi_1\rangle\langle 0| + |\phi_2\rangle\langle 1|.$$

The final optimized circuit is shown in figure 6(b).

(a) Unoptimized



(b) Optimized

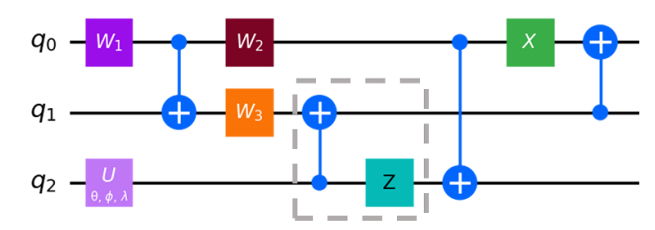


Figure 6. State preparation circuits for DFS₃ encoding. Panel (a) shows the unoptimized circuit expressed in terms of controlled gates CG_1 and CG_2 . The optimized circuit resulting from a Schmidt decomposition is displayed in panel (b). The gates encapsulated by the gray, dashed box are only implemented if the gauge qubit (q2) is not prepared in $|0\rangle$.

Appendix B. DFS₂ DD protocol

The DD sequence in equation (10) generates collective dephasing up to first-order in time-dependent perturbation theory. The sequence can achieve this suppression condition for general two-qubit system-environment interactions of the form

$$H_{SB} = \sum_{\alpha_1, \alpha_2} (\sigma_1^{\alpha_1} \sigma_2^{\alpha_2}) \otimes B^{\alpha_1 \alpha_2}, \ \alpha_i \in \{0, x, y, z\},$$
 (B1)

where $B^{\alpha_1\alpha_2}$ denotes a bounded bath operator coupled to the system. The interaction Hamiltonian can be rewritten as

$$H_{\rm SB} = H_{\rm Leak} + H_{\rm Logi} + H_{\rm DFS}, \tag{B2}$$

where $H_{\text{Leak}} = \text{span}(\mathcal{P}_{\text{Leak}})$ denotes leakage errors, i.e. terms that cause transitions between states inside and outside of the DFS. The Hamiltonian $H_{\text{Logi}} = \text{span}(\mathcal{P}_{\text{Logi}})$ includes operators that form undesirable logic gates on the DFS that couple to the bath and cause decoherence. Lastly, $H_{\text{DFS}} = \text{span}(\mathcal{P}_{\text{DFS}})$ designates operators that either vanish or are proportional to identity on the DFS. The spanning subspaces for each Hamiltonian, in terms of the two-qubit Pauli basis are

$$\begin{split} \mathcal{P}_{\text{Leak}} &= \{\sigma_1^x, \sigma_2^x, \sigma_1^y, \sigma_2^y, \sigma_1^x \sigma_2^z, \sigma_1^z \sigma_2^x, \sigma_1^y \sigma_2^z, \sigma_1^z \sigma_2^y\} \\ \mathcal{P}_{\text{Logi}} &= \{\bar{\sigma}^x, \bar{\sigma}^y, \bar{\sigma}^z\} \\ \mathcal{P}_{\text{DFS}} &= \left\{ \frac{\sigma_1^z + \sigma_2^z}{2}, \frac{\sigma_1^x \sigma_2^y + \sigma_1^y \sigma_2^x}{2}, \frac{\sigma_1^x \sigma_2^x + \sigma_1^y \sigma_2^y}{2}, \frac{I_4, \sigma_1^z \sigma_2^z\}, \right. \end{split} \tag{B3}$$

where I_4 is the two-qubit identity operator and the logical operators in $\mathcal{P}_{\text{Logi}}$ are defined in equation (3).

Following [71], it can be shown that logical operations can be used to design DD sequences that suppress all terms acting non-trivially on the DFS. Specifically, the sequence shown in equation (10) utilizes a concatenation of three sub-sequences that together suppress H_{Leak} and H_{Logi} in the ideal, instantaneous pulse limit. Each sub-sequence contains two pulses separated by free evolution periods of duration τ . As such, the generic construction of the sub-sequences can be defined by $U \circ f_{\tau} \equiv U f_{\tau} U^{\dagger} f_{\tau}$, where $f_{\tau} = e^{-iH_{\text{SB}}\tau}$. Note that $\Pi = \bar{R}_x(\pi)$ anticommutes with $\mathcal{P}_{\text{Leak}}$, so it suppresses leakage out of the DFS. The logical operators $\bar{Y} = \bar{R}_y(\pi/2)$ and $\bar{X} = \bar{R}_x(\pi/2)$ can be used to suppress $\mathcal{P}_{\text{Logi}}$ via a standard XY4 sequence, i.e. a concatenation of \bar{X} and \bar{Y} . The concatenation of the leakage suppression and logical error suppression sequences yields the following sequence:

$$\bar{Y} \circ \bar{X} \circ \Pi \circ f_{\tau}
= \bar{Y} \circ \bar{X} \circ (\Pi f_{\tau} \Pi^{\dagger} f_{\tau})
= \bar{Y} \circ [\bar{X} (\Pi f_{\tau} \Pi f_{\tau}) \bar{X}^{\dagger} (\Pi f_{\tau} \Pi f_{\tau})]
= \bar{Y} \bar{X}^{\dagger} f_{\tau} \Pi f_{\tau} \bar{X} f_{\tau} \Pi f_{\tau} \bar{Y}^{\dagger} \bar{X}^{\dagger} f_{\tau} \Pi f_{\tau} \bar{X} f_{\tau} \Pi f_{\tau},$$
(B4)

where in the last line we used $\Pi = \Pi^{\dagger}$ along with $\bar{X}\Pi = \bar{X}^{\dagger}$ and $\bar{X}^{\dagger}\Pi = \bar{X}$.

Appendix C. Implementation of DFS₂ DD pulses

The DD sequence used to generate the collective dephasing DFS requires logical operations $\bar{R}_x(\theta)$ and $\bar{R}_y(\theta)$. These logical unitaries are generated by logical operators $\bar{\sigma}^x$ and $\bar{\sigma}^y$, respectively, which can take many forms. Belonging to the commutant of the error algebra only requires that the Hermitian operators be expressed as a linear combinations of the identity, σ_i^z , $\sigma_1^z\sigma_2^z$, and $\bar{\sigma}_1 \cdot \bar{\sigma}_2 = \sigma_1^x\sigma_2^x + \sigma_1^y\sigma_2^y + \sigma_1^z\sigma_2^z$. The operators given in equation (3) define symmetric logical operators that satisfy the so-called independence property [79] (i.e. they act entirely within the specified DFS) and preserve *all* DFSs in the two-qubit Hilbert space [83]. Hence, operators on the logical subspace defined by $\{|01\rangle, |10\rangle\}$ do not enable mixing between the one-dimensional subspaces defined by $|00\rangle$ and $|11\rangle$. While alternative, non-preserving logical operators, such as

$$\bar{\sigma}^x = \sigma_1^x \sigma_2^x$$

$$\bar{\sigma}^y = \sigma_1^x \sigma_2^y + \sigma_1^y \sigma_2^x$$

$$\bar{\sigma}^z = -\sigma_2^z$$
(C1)

can be defined, empirical evidence shows that the symmetric operators yield higher fidelities.

The preference towards the symmetric operators is quite surprising considering that their gate decomposition requires twice as many CNOT operators. This can be seen by utilizing commutativity to decompose the logical operators into products of two-local rotation operators. For example,

$$\bar{R}_{x}(\theta) = e^{-i\theta/2\sigma_{1}^{x}\sigma_{2}^{x}}e^{-i\theta/2\sigma_{1}^{y}\sigma_{2}^{y}}, \tag{C2}$$

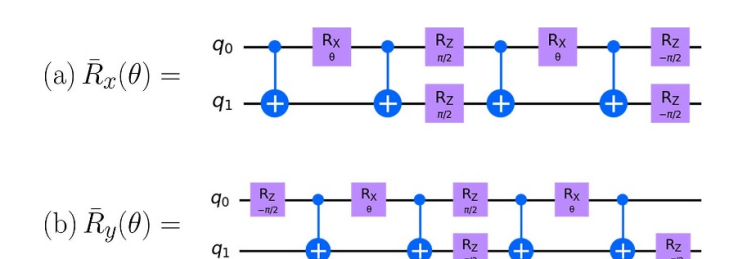


Figure 7. Decompositions for the symmetric logical rotation gates in terms of the IBMQP gateset. (a) shows the logical *x*-rotation gate, while the logical *y*-rotation gate is given in (b).

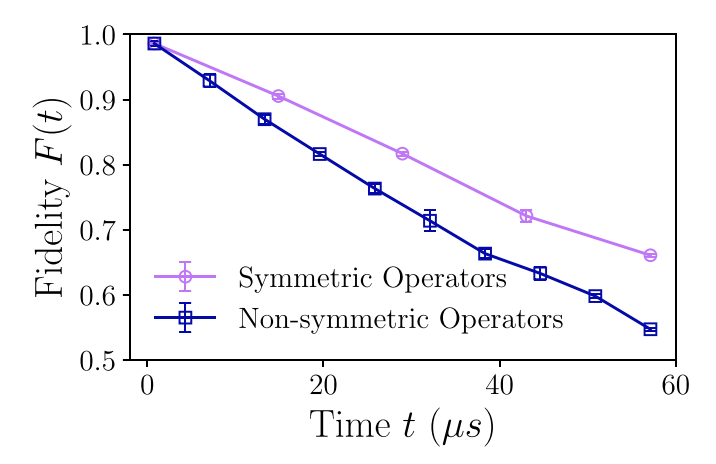


Figure 8. Comparison of different logical operator definitions for the DFS $_2$ +DD protocol. Symmetric logical operations yield higher fidelity than the non-symmetric case. Demonstrations are performed on the 5-qubit IBMQP Manila device, with data points and error bars denoting means and CIs, respectively. Bootstrapping over five realizations of the demonstration is employed to calculated statistical quantities. 8000 shots are used per demonstration execution.

where each two-qubit interaction unitary can be decomposed into single qubit rotations bookended by CNOT gates; see figure 7(a). Following a similar decomposition, one obtains the circuit for $\bar{R}_y(\theta)$ in terms of the IBMQP gateset $\mathcal{G} = \{X_{\pi/2}, X_{\pi}, R_z(\theta), \text{CNOT}\}$ as shown in figure 7(b). The average logical gate time across the five data collection periods was $1.47 \pm 0.30 \mu \text{s}$ on the 5-qubit Manila device. The average logical gate time for the 27-qubit Montreal device was $1.67 \pm 0.33 \mu \text{s}$.

Note that the definitions of non-symmetric logical operators yield unitaries similar to the first two-local interaction in the symmetric decomposition. For example, the non-symmetric logical x-rotation operator is $\bar{R}_x(\theta) = e^{-i\theta\sigma_1^x\sigma_2^x}$, which only requires two CNOT gates when decomposed via \mathcal{G} . Despite the reduction in gate time and depth, the non-symmetric operators do not outperform their symmetric counterparts; see figure 8.

Moreover, we do not observe improved performance from optimizing the gate decompositions of the symmetric logical operators. The decompositions given in figure 7 utilize four CNOTs, one more than what should be required for the decomposition of any two-qubit gate [90]. However, we find that

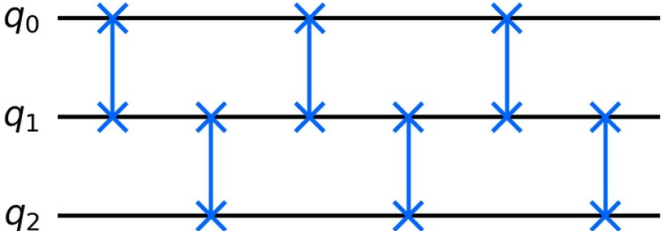


Figure 9. NS symmetrization sequence consisting of six SWAP operations. Each SWAP gate is decomposed into three CNOT gates when implemented on IBMQP processors. The timing between gates follows equation (11) with $\tau=0$. Implementation of the gates, however, is subject to the control timing resolution. As such, the true inter-pulse delay is $\tau_{\text{true}}\approx 0.2$ ns.

optimizing the number of CNOT gates does not lead to better performance. We suspect that the four CNOT gate decomposition permits some form of inherent noise robustness not afforded by the optimized variation. Further investigation of the inherent hardware noise model is needed to fully understand this effect.

Appendix D. FS₃ DD protocol

The collective decoherence condition for the DFS₃ code can be generated by the DD sequence shown in equation (11). This sequence is sufficient to symmetrize any linear systemenvironment interaction of the form

$$H_{\rm SB} = \sum_{i=1}^{3} \vec{\sigma}_i \cdot \vec{B}_i,\tag{D1}$$

where $\vec{B}_i = (B_i^x, B_i^y, B_i^z)$ and B_i^μ are bounded bath operators. In the ideal, instantaneous pulse limit, the dynamics after the sequence are governed by an effective Hamiltonian of the form $H_{\rm eff} = (\sum_i \vec{\sigma}_i) \cdot \vec{B}' + \mathcal{O}(\tau^2)$, where τ is the duration of free evolution between pulses and $\vec{B}' = 2(\vec{B}_1 + \vec{B}_2 + \vec{B}_3)$. This result can be shown by writing the sequence as

$$U(T = 6\tau) = \prod_{i=1}^{6} P_{j}^{\dagger} f_{\tau} P_{j},$$
 (D2)

and computing the first-order term in the Magnus expansion with

$$P_j \in \{I, E_{12}, E_{12}E_{23}, E_{13}, E_{12}E_{13}, E_{23}\}.$$
 (D3)

Note that equation (D2) can be reconciled with equation (11) by using $E_{23} = E_{12}E_{13}E_{12} = E_{13}E_{12}E_{13}$ and $E_{12} = E_{23}E_{12}E_{13}$. The sequence's circuit diagram is shown in figure 9. Note that the inter-pulse delay τ is effectively set to zero in our experiments. Due to control hardware, however, the true delay time set is $\tau_{\text{true}} = \delta t$, where $\delta t \approx 0.2$ ns is the time resolution of the controller.

It is important to note that the sequence used in this study is not the only choice. An alternative originally proposed in [69] also enables collective decoherence at the cost of 14 SWAP gates. Equation (11) utilizes only 6 pulses while still achieving the same first-order effect.

Appendix E. Post-selection protocols

Aiming to exploit the stabilizer properties of the DFS codes used in this study, we identify PS procedures to discard a subset of states corresponding to detectable errors. Ideally, conditioning the measurement outcomes on the state of the ancilla qubits ultimately results in a boosted fidelity for the data qubit. Here, we elaborate on the PS procedure used for both the two-and three-qubit codes.

We begin by formally calculating the state after measurement. Consider the case where a logical DFS_N state $\rho_L(0) = |\psi_L\rangle\langle\psi_L|$ is prepared and then subject to an error channel \mathcal{E}_P . Let this error channel be a composition of channels $\mathcal{E}_P = \mathcal{E}_{P_N} \circ \cdots \circ \mathcal{E}_{P_1}$, where

$$\mathcal{E}_{P_i}(\rho) = (1 - p_i) \rho + p_i P_i \rho P_i^{\dagger}$$
 (E1)

acts on the *i*th qubit and p_i is the error probability. The error operator P_i is assumed to be a single-qubit Pauli operator and thus inherently satisfies the required completeness relation to be trace-preserving.

Subjecting the logical DFS state to the error channel results in

$$\tilde{\rho}_{L} = \mathcal{E}_{P}(\rho_{L}(0))$$

$$\approx \tilde{p}_{0}\rho_{L}(0) + \sum_{i=1}^{N} \tilde{p}_{i}P_{i}\rho_{L}(0)P_{i}^{\dagger}, \tag{E2}$$

where the approximation is valid in the weak noise limit, i.e. $p_i \ll 1 \ \forall i$. The effective error rates are $\tilde{p}_i = p_i \prod_{j \neq i} (1 - p_j)$, with $\tilde{p}_0 = \prod_{i=1}^N (1 - p_i)$. Measurement outcomes are determined by first applying the unitary U_{dec} to decode the state. This is followed by a measurement of each qubit in the computational basis via a composition of maps $\mathcal{E}_M = \mathcal{E}_M^{(N)} \circ \cdots \circ \mathcal{E}_M^{(1)}$, with $E_M^{(i)}(\rho) = E_0^{(i)} \rho E_0^{(i)\dagger} + E_1^{(i)} \rho E_1^{(i)\dagger}$. The projection operators $E_0^{(i)} = |0\rangle\langle 0|$ and $E_1^{(i)} = |1\rangle\langle 1|$ act on the ith qubit. Note that we have assumed ideal measurement on each qubit.

The resulting density operator can be expressed as

$$\tilde{\rho}_{\text{dec}} = \mathcal{E}_{M} \left(U_{\text{dec}} \mathcal{E}_{P} \left(\rho_{L}(0) \right) U_{\text{dec}}^{\dagger} \right)$$

$$\approx \tilde{p}_{0} |\mathbf{0}\rangle\langle\mathbf{0}| + \sum_{i=1}^{N} \tilde{p}_{i} \sum_{k} e_{i,k} |k\rangle\langle k|. \tag{E3}$$

The first contribution results from perfect decoding of the state back to $|\mathbf{0}\rangle = |0\cdots 0\rangle$. The second term arises from projections onto the computational basis states $|k\rangle \in \mathcal{H}_S$. The presence of these states is determined by the resulting overlap $e_{i,k} = \langle k|U_{\rm dec}P_i\rho_L(0)P_i^{\dagger}U_{\rm dec}^{\dagger}|k\rangle$, which depends upon the underlying noise channel. As we will show below, the error state distributions for the DFS can be distinguished based on the type of error considered.

E.1. DFS₂ protocol

The DFS₂ code can detect single-qubit bit-flip errors. We use the expressions above to investigate the error states resulting from such errors by selecting $P_i = \sigma_i^x$. Single-qubit bit-flip errors can be shown to result in the state $|01\rangle$. Thus, detectable errors are those in which the ancilla qubit has flipped upon decode and measurement. We exploit this fact and condition the measurement outcomes on the ancilla qubit remaining in the ground-state at the end of the demonstration. Notably, a similar analysis can be performed for higher weight errors as well. As expected, we find that weight-2 bit-flip errors result in phase-flip errors that are not detected and thus, do not result in a unique error state. Furthermore, it is important to note that $|10\rangle$ does not appear as an error state in the analysis since we have neglected phase flip errors. Performing a similar analysis with $P_i = \sigma_i^z$ reveals this additional error state.

E.2. DFS₃ protocol

The three-qubit code provides detection of an odd number of bit and phase-flips. Thus, ideally, the PS procedure would account for both types of errors simultaneously. In devising our procedure, we first examine weight-1 errors for $P_i = \sigma_i^x$ and $P_i = \sigma_i^z$. The set of error states are

$$S_1^X = \{|100\rangle, |110\rangle, |101\rangle, |111\rangle\},$$

$$S_1^Z = \{|010\rangle, |001\rangle, |011\rangle\},$$
(E4)

where $|q_0q_1q_2\rangle$ defines the qubit layout with q_1 denoting the data qubit. Albeit quite distinct, states that correspond to errors on the data qubit (i.e. $q_1=1$) tend to have a common ancilla qubit bit-flip on q_0 or q_2 . Naively, one may come to the conclusion that conditioning the measurement outcomes on both ancilla qubits being in the ground state would, therefore, be a reasonable PS criterion. However, this criterion also results in the discarding of states where the data qubit correctly returns to the ground state. Based on empirical evidence, which we further elaborate on in appendix I.1, we find that a reasonable balance between discarded error states and correct data qubit states is achieved by conditioning the measurement outcomes on $q_2=0$.

For completeness, we can further characterize higher weight errors. We find that weight-2 and weight-3 bit-flip errors have the following error signatures:

$$\mathcal{S}_2^X = \{|001\rangle, |010\rangle, |011\rangle\}$$

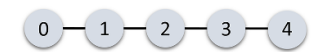
$$\mathcal{S}_3^X = \{|100\rangle, |110\rangle, |101\rangle\}.$$
(E5)

In contrast, $S_2^Z = S_3^Z = S_1^Z$; thus, regardless the weight, phase-flip errors have identical error states.

Appendix F. Hardware specifications

All demonstrations were performed on the IBMQP, a cloudbased quantum computing resource that offers access to superconducting transmon quantum processors. All circuits were

Manila



Montreal

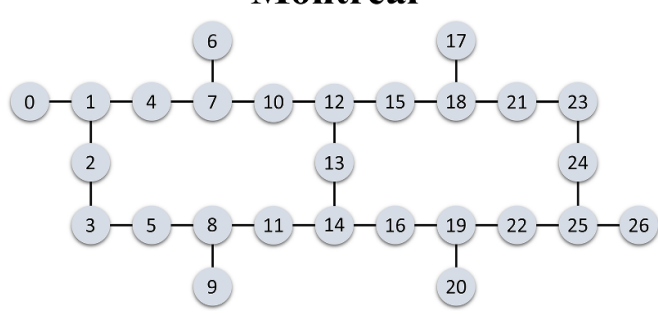


Figure 10. Connectivity graphs for the 5-qubit IBMQP Manila (top) and 27-qubit Montreal (bottom) devices.

Table 2. Device specification for Manila and Montreal. QV and CLOPS denote quantum volume and circuit layer operations per second, respectively.

Device	Manila	Montreal
Processor	Falcon r5.11L	Falcon r4
QV	32	128
CLOPS	2.8 K	2.7 K

Table 3. Physical parameters for the Manila device averaged over five realizations of demonstrations collected during 20–25 September, 2022. Uncertainties denote one standard deviation.

Qubit	$T_1 (\mu s)$	$T_2 (\mu s)$	1Q Gate Error ($\times 10^{-3}$)	Readout Error $(\times 10^{-2})$
0	120.8 ± 25.0	71.3 ± 18.4	0.31 ± 0.11	2.93 ± 0.65
1	173.9 ± 42.9	68.9 ± 6.6	0.22 ± 0.01	2.57 ± 0.26
2	136.6 ± 20.4	26.0 ± 2.0	0.31 ± 0.04	2.50 ± 0.30
3	200.0 ± 20.6	60.4 ± 6.3	0.20 ± 0.02	2.54 ± 0.25
4	148.7 ± 17.0	43.0 ± 1.3	0.49 ± 0.07	3.51 ± 1.42

Table 4. CNOT gate error rates and durations for specific control (C) and target (T) qubits for Manila. Values denote averages with one standard deviation determined from calibration data collected during 20–25 September, 2022. Reversing control and target qubits requires an additional single qubit gate that increases the gate time by 35 ns and effectively increases the error rate based on table 3.

Qubits (C,T)	CNOT Error Rate $(\times 10^{-3})$	CNOT Duration (ns)
(0,1)	6.91 ± 0.23	277.33
(1,2)	13.78 ± 4.06	469.33
(2,3)	7.61 ± 1.53	355.55
(4,3)	5.61 ± 0.82	298.67

written in Python using the Qiskit API created by IBM. We used the 5-qubit Manila and 27-qubit Montreal devices in our experiments. Each processor's connectivity graph is shown in figure 10. The processor type, quantum volume (QV), and circuit layer operations per second (CLOPS) are detailed in table 2.

Qubit characteristics, such as T_1 , T_2 times, gate error rates, readout error rates, and gate durations for each device are presented in tables 3 and 4. In all cases, qubit

characteristics are collected over the duration of data collection, i.e. five realizations of each demonstration collected over multiple days. Values shown in the tables denote averages with error bars indicating one standard deviation.

Qubit characteristics for Manila are shown in tables 3 and 4 for experiments performed during 20–25 September, 2022. T_1 typically ranges from 120.8 μ s to 200 μ s, whereas T_2 varies from 43 μ s to 71.3 μ s. Single qubit gate error rates are on the

Table 5. Qubit characteristic timescales and error rates for Montreal. Data shown for qubits used in demonstrations only. Averages and error bars (one standard deviation) determined from calibration data collected 11–20 October, 2022.

Qubit	T_1 (μ s)	$T_2 (\mu s)$	1Q Gate Error (×10 ⁻³)	Readout Error $(\times 10^{-2})$
0	96.3 ± 14.2	38.2 ± 10.4	0.19 ± 0.02	1.10 ± 0.12
1	99.5 ± 13.8	22.7 ± 0.8	0.21 ± 0.06	1.63 ± 0.41
2	87.2 ± 7.1	106.5 ± 6.4	0.32 ± 0.1	1.39 ± 0.38
3	80.3 ± 4.1	71.5 ± 3.5	0.2 ± 0.02	0.93 ± 0.09
4	76.8 ± 8.6	104.7 ± 13.0	0.24 ± 0.07	1.57 ± 0.36
5	85.5 ± 7.1	95.5 ± 11.6	0.27 ± 0.18	1.21 ± 0.64
7	75.3 ± 14.8	67.2 ± 11.2	0.55 ± 0.11	5.36 ± 0.82
8	95.1 ± 13.7	120.4 ± 9.0	0.27 ± 0.08	1.14 ± 0.13
9	86.9 ± 7.6	107.6 ± 9.9	0.26 ± 0.03	1.02 ± 0.29
10	86.5 ± 17.6	86.3 ± 9.8	0.32 ± 0.07	0.82 ± 0.15
11	93.5 ± 5.3	60.9 ± 9.8	0.22 ± 0.04	1.53 ± 0.31
12	101.9 ± 10.9	140.0 ± 26.8	0.29 ± 0.08	2.02 ± 0.51
13	58.9 ± 18.9	55.6 ± 11.0	0.35 ± 0.09	1.34 ± 0.31
14	79.4 ± 17.4	100.2 ± 24.0	0.41 ± 0.27	1.08 ± 0.3
15	97.8 ± 4.3	121.3 ± 9.6	0.39 ± 0.17	1.81 ± 0.75
16	82.2 ± 5.9	87.3 ± 4.7	0.3 ± 0.13	1.24 ± 0.82
18	73.7 ± 12.6	28.7 ± 2.2	0.46 ± 0.17	3.14 ± 0.73
19	89.9 ± 5.6	137.8 ± 17.9	0.24 ± 0.15	1.11 ± 0.29
21	105.2 ± 11.3	50.6 ± 5.4	0.51 ± 0.1	3.53 ± 0.56
23	55.6 ± 24.4	55.9 ± 18.0	0.41 ± 0.35	2.03 ± 1.44
24	79.5 ± 7.5	56.9 ± 3.6	0.32 ± 0.09	2.41 ± 1.34

order of 10^{-4} and readout error rates on the order of 10^{-2} . In table 4, specifications for CNOT gate error rates and durations are shown to range from 5.61×10^{-3} to 13.78×10^{-3} and approximately 277 to 469 ns. Data is shown for control-target qubit pairs where the gate duration is shorter. Reverse ordering will incur an additional single qubit gate that increases both the error rate in accordance with table 3 and gate duration by approximately 35.55 ns.

A similar set of data for Montreal is shown in tables 5 and 6. We show data specifically for the qubits used in the demonstrations. Averages and standard deviations are determined from calibration data collected during 11–20 October, 2022. Qubit relaxation and dephasing times vary across the device as $55.6-105.2~\mu s$ and $22.7-140.0~\mu s$, respectively. Similar to Manila, single qubit gate error rates are on the order of 10^{-3} and CNOT error rates are on the order of 10^{-3} . Readout error rates are on the order of 10^{-2} for a majority of the qubits used in the demonstrations. Variations in CNOT gate error rates are accompanied by varying duration for a significant subset of qubits; see table 6.

Appendix G. Data collection and analysis

G.1. Data collection practices

The IBMQP devices are subject to recalibration every few hours. During calibration, the characterization of qubit transition frequencies, error rates, and decoherence times are performed alongside updates to single-qubit and two-qubit pulse waveforms. We observe that qubit performance can vary significantly between, and even within, calibration cycles. Fluctuations in qubit characteristic parameters typically manifest as large shifts in fidelity when data is collected across calibrations. Furthermore, variations in the fidelity are observed depending upon when one performs the experiment. For example, experiments performed soon after a calibration can be distinct from those performed just before a calibration. While this variability is likely due to drift in qubit frequencies and/or the control master clock, knowledge of the potential origin of the errors does not necessarily imply that it is straightforward to mitigate.

Our demonstrations require a large suite of quantum circuits to be executed and thus, we are subject to data collection across multiple calibration cycles. In order to address the effects of hardware variability, we incorporate three practices in our circuit execution. Let us describe each practice by first defining a demonstration $D = \{C_j\}_{j=1}^N$ consisting of N sets of circuits C_j . Each set $C_j = \{c_{j,k}\}_{k=1}^K$ is composed of K circuits each of approximately equivalent total time T_j . For example, D could describe a DD experiment where N different DD repetitions are applied and C_j consists of different DD sequences of equivalent total time.

The first practice is intrinsic to the definition of D. During circuit creation, we organize the circuits such that those with the same total time are performed immediately after each other; hence, C_j . In this manner, we aim to mitigate potential variability in the hardware noise environment as data is collected for different error protection protocols at the same T_j . In addition, the order in which circuits are implemented is randomized with respect to j. For example, a demonstration consisting of N = 4 total times may be executed on hardware in the following order: C_3 , C_1 , C_2 , C_4 . We find that this approach effectively averages variability due to calibrations across all

Table 6. CNOT error rates and durations for IBMQP Montreal for qubits used in demonstrations. Average calibration values shown for data collected 11–20 October, 2022. Error bars denote one standard deviation.

Qubits (C,T)	CNOT Error Rate $(\times 10^{-3})$	CNOT Duration (ns)	
(0,1)	7.6 ± 3.95	412.08 ± 44.8	
(3,2)	7.53 ± 1.12	375.79 ± 9.6	
(1,4)	10.19 ± 2.7	492.13 ± 54.4	
(5,3)	7.4 ± 1.8	350.63 ± 19.2	
(4,7)	13.37 ± 4.49	294.47 ± 16.0	
(9,8)	5.97 ± 0.85	373.79 ± 6.4	
(11,8)	7.8 ± 1.87	470.06 ± 35.2	
(12,10)	6.49 ± 0.66	374.88 ± 3.2	
(13,14)	12.37 ± 5.59	502.7 ± 19.2	
(15,12)	9.58 ± 2.1	369.78 ± 0.0	
(16,14)	9.89 ± 3.43	309.97 ± 16.0	
(15,18)	18.62 ± 7.05	597.33	
(16,19)	13.70 ± 2.35	270.22	
(23,21)	12.50 ± 3.61	391.11	
(23,24)	10.28 ± 2.87	397.31 ± 12.8	

 T_j rather than isolating it to specific total times. Lastly, multiple realizations (or replications) of each demonstration are executed over many hours or even days to collect data under a variety of hardware conditions. The data is then compiled and used to estimate various statistical quantities via bootstrapping. We find that this approach enables a more reliable estimate of an error protection protocol's performance.

G.2. Bootstrapping

The results reported in the main text display the mean and confidence intervals estimated via the bootstrapping method described in [98]. This technique is implemented by randomly sampling N data points (with replacement) from a data set of size N and then computing the mean of this bootstrapped sample. By repeating this procedure K times, a new, bootstrapped data set of size K is generated. The mean and confidence interval (CI) can be calculated based on this bootstrapped data set. This approach is used to estimate mean fidelities and CIs for equations (12), (15), and (18), which are used in the comparisons shown in figures 2–5.

G.3. Fitting protocol

Data fits are performed for fidelity vs. time comparisons shown in figure 4. Bootstrapped estimates of fidelity are fit to the generic fit equation given in equation (16). Parameter reductions of the fit equation are also considered, most notably in cases where generic fits suggest parameters are inconsequential. Various fits derived from equation (16) are compared using the Akaike information criterion (AIC) [99], an estimator of prediction error. Fits shown in the main text correspond to the cases where AIC is minimal among the fit variations considered.

Appendix H. DFS₃ logical state asymmetry

In section 3.1, the DFS₃ encoding is shown to exhibit an asymmetry in fidelity as a function of the elevation angle θ . This feature is particularly prominent for the logical encoding without DD. Here, we argue that this behavior is in part due to non-uniform detuning among the physical qubits on the IBM processors [46, 95, 96].

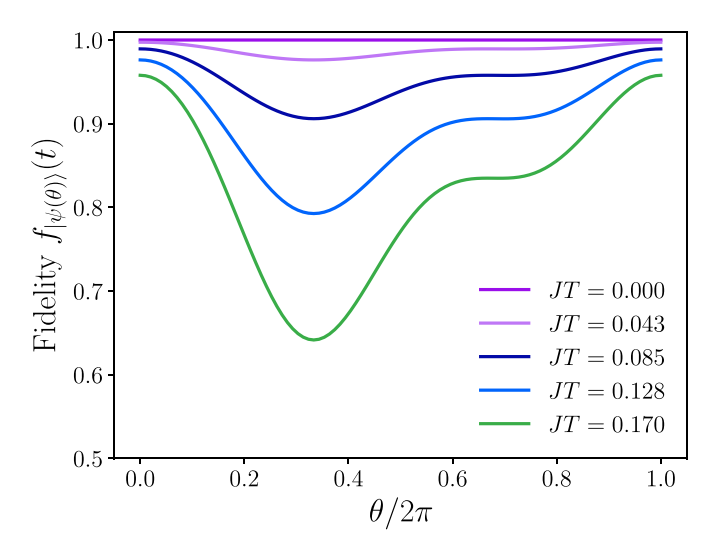


Figure 11. Simulation of DFS₃ subject to non-uniform detuning. The logical qubit is prepared according to $|\psi_L(\theta)\rangle$ (see section 3.1) and then evolved via the Hamiltonian described in equation (H1). The fidelity [calculated via equation (12)] as a function of the elevation angle θ conveys an asymmetry in the initial state. This effect, in part, is suspected to contribute to the asymmetry observed in figure 2.

In figure 11, we display a comparison of fidelity as a function of θ for the DFS₃ code. The system is prepared in the logical state $|\psi_L(\theta)\rangle$ as described in section 3.1. It is then

subject to the evolution $U(T) = e^{-iH_dT}$, where

$$H_d = \sum_{i=1}^{3} \omega_i \, \sigma_i^z, \tag{H1}$$

with $\omega_1 = \pi/2$, $\omega_2 = \pi/4$, and $\omega_3 = \pi$. The fidelity is then determined via equation (12) without PS.

The comparison is performed for various Hamiltonian strengths $J = \|H_d\|_{\infty}$, where $\|\cdot\|_{\infty}$ denotes the operator norm or largest singular value. The total time is set to T=1. As the strength of the detuning Hamiltonian increases, the asymmetry in the fidelity becomes more pronounced for $\theta \in [0.1, 0.6]$ as observed in figure 2. Although the model is able to capture general features of the asymmetry, it is not sufficiently expressive to capture all fluctuations in the fidelity. Further modeling is required to obtain an in-depth understanding of the observed dynamics; this is left for future work.

Appendix I. Post-selection analysis

A crucial component for the success of the DFS codes is the use of post-selection (PS) to detect errors in the logical states. In the DFS₂ protocol, post-selected states are aggregated based on the state of the ancilla qubit. Namely, combined two-qubit states in which the ancilla returns to the ground state after decoding are deemed viable. In the DFS₃ code, the gauge qubit (q_2 in figure 6) is used to identify valid states. In this section, we examine PS from a variety of different viewpoints to highlight its impact on fidelity and protocol resources.

I.1. State-dependence

The impact of PS on fidelity is strongly dependent upon the logical state and encoding. In the case of the DFS $_2$ code, only minor improvements in fidelity are found when using PS without error suppression. States near the $|+\rangle$ state are particularly enhanced by PS, as can be seen in figure 12(a). Near equivalent fidelity between the DFS with and without PS suggests that the logical states are predominately plagued by logical errors or bit-flip errors rather than detectable single qubit phase-flip errors. Through DD, the logical fidelity greatly improves on average, and similarly, so does the effectiveness of error detection. The reduction of the logical error rate enables detectable errors to become more pronounced so that PS yields an average increase in the fidelity of 6.1%; see figure 12(c).

The DFS $_3$ code offers a striking contrast to the DFS $_2$ code when DD is not employed. States near $|0\rangle$ of the logical Bloch sphere are highly susceptible to noise that error detection can reduce considerably. Conversely, states between logical $|\pm\rangle$ are negatively impacted by PS; see figure 12(b). The source of this behavior can be revealed by examining the measurement outcome distributions.

In figure 13, the measured state probability distributions are shown for the DFS₃ code and DFS₃+DD. Panels (a) and (b) convey the distributions for the DFS₃ code at elevation

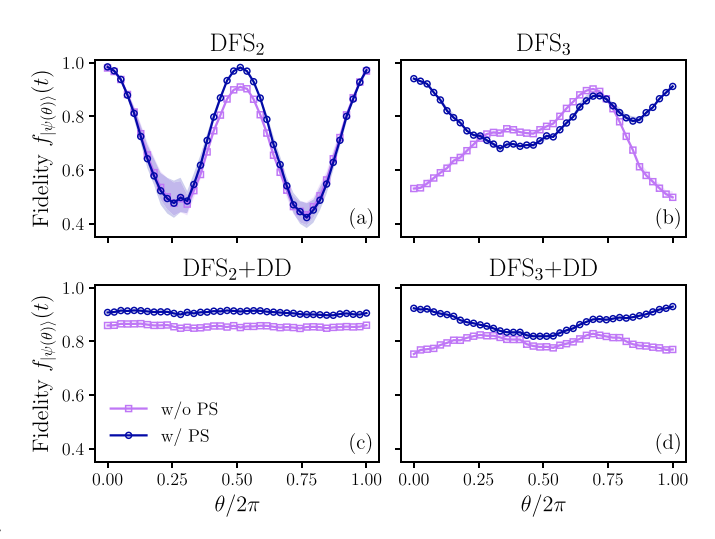


Figure 12. Fidelity as a function of initial state for DFS encodings with and without PS. Panels (a) and (b) denote DFS₂ and DFS₃ encodings alone, respectively. Encodings with DD are shown in panels (c) and (d). The most prominent impact on fidelity is observed for the DFS₃ case, specifically states that are near the poles of the logical Bloch sphere. Data points denote means and shaded regions are CIs. Statistical quantities are estimated from bootstrapping over five realizations of the demonstration using 8000 shots.

angles $\theta=0$ and $\theta=\pi/2$, respectively. Importantly, for $\theta=0$, we observe that the errors predominately originate from discarded error states (shown in dark blue); hence, the significant improvement in fidelity when utilizing PS. Error states become increasingly distributed after reaching logical $|+\rangle$, such that the PS procedure has less of a positive impact on qubit fidelity.

Despite the distinctions between the DFS₂ and DFS₃ codes, as shown in figure 12(d), similarities re-emerge upon the introduction of DD. Symmetrization leads to an overall improvement in logical state fidelity and detectable errors. On average, PS yields a 9.7% improvement in the DFS₃+DD fidelity, with deviations from uniform fidelity being corroborated with the error distributions shown in figures 13(c) and (d). Namely, near $|0\rangle$ the errors primarily fall within the discarded error states, while those for $\pi/2 < \theta < \pi$ are more distributed among PS and discarded error states.

I.2. Time-dependence

Investigating the effectiveness of PS as a function of time provides an alternative perspective on each protection protocol. In this section, we study the number of post-selected shots and state-averaged fidelity as a function of time. The former is shown in figure 14, while the latter is displayed in figure 15. Both are produced from the same data set used to create figure 4 in the main text; hence, they focus on the time-dependent state preservation of a single logical qubit.

The cost of PS is a reduction in the total number of experimental measurements (or shots) that can be used to estimate state fidelity. Figure 14 illustrates the cost for each code with and without DD. Interestingly, DD does not always increase

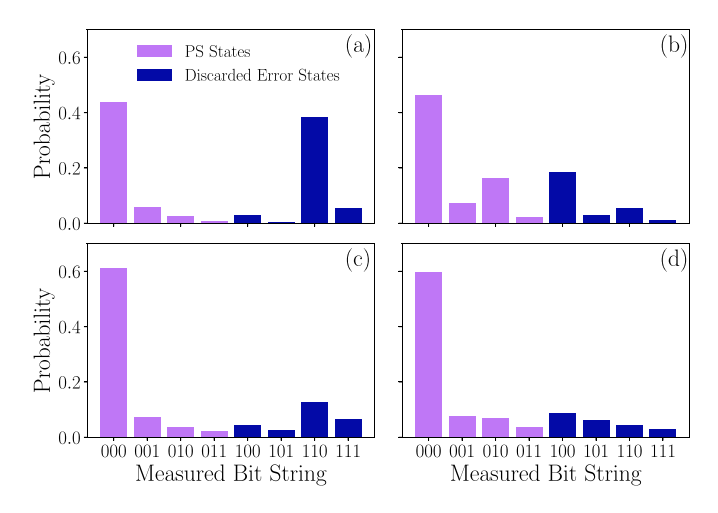


Figure 13. Measured state probability distributions for the DFS₃ code [(a) and (b)] and the DFS₃+DD protocol [(c) and (d)] for the data shown in figure 12. The distributions for $\theta=0$ are shown in panels (a) and (c), while (b) and (d) display distributions for $\theta=\pi/2$. Measured bit strings are ordered as $q_2q_1q_0$ following the qubit layout shown in figure 6. States are categorized as PS states $(q_2=0;$ purple) and discarded error states $(q_2=1;$ dark blue). Results indicate that high probability discarded error states are typically associated with phase errors.

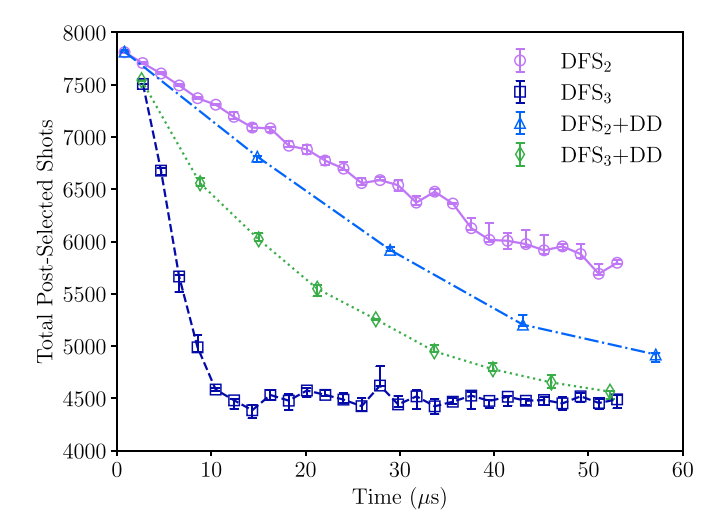


Figure 14. Total number of post-selected shots used to determine the state-averaged fidelity in figure 4 as a function of time. Markers denote means, and error bars denote CIs, both of which are determined by bootstrapping. Overall, we observe that the inclusion of DD negatively impacts the PS shot count for the DFS₂ code, while improving the number of viable shots for the DFS₃ code. Despite this behavior, DD has an overall positive effect on code performance as it reduces logical errors, i.e. errors not detected by PS.

the total number of viable shots. In the case of the two-qubit protocol, the total number of post-selected shots reduces more slowly with the DFS alone. After one cycle of DD, the quantity of PS shots reduces by approximately 4%. Of course, this does not imply an increase in state fidelity due to the presence of logical errors, as is indicated by figure 4. DD with PS is still

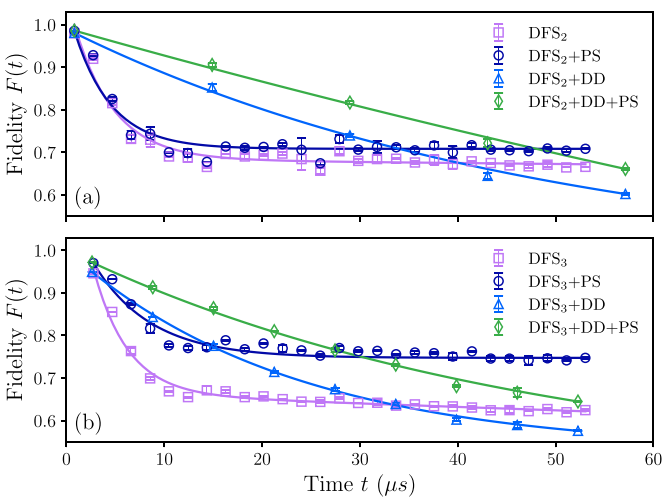


Figure 15. State-averaged fidelity as a function of time for one logical qubit. Panels (a) and (b) show results for the DFS₂ and DFS₃ codes, respectively. Data and fits are shown for each code with PS, DD, or both. The results shown here supplement those shown in figure 4, where the data was used to calculate the time-averaged fidelity in the short- and long-time limits. Data points denote means while error bars denote CIs, both obtained from bootstrapping over five experimental data sets, each using 8000 measurement shots.

more advantageous than PS alone but ultimately requires more shots to achieve a particular sampling threshold.

The three-qubit DFS code contrasts with the two-qubit case. Specifically, the DFS₃ code benefits from DD in regards to the total number of PS shots. The DFS₃ code alone is subject to a dramatic reduction after approximately 10 μ s, where only about half of the total shots satisfy the PS criteria. DD affords a substantial improvement, increasing the total PS shot counts by over 31%. As such, PS and DD improve the total viable shot count and fidelity.

Despite the dissimilarity in total PS shot count between the codes, the trend in fidelity is universal: DD and PS used together typically supply the greatest positive impact on code performance. In figure 15, the state-averaged fidelity as a function of time is shown for each code under a variety of conditions. The data shown in each panel is used to produce the time-averaged fidelity shown in figure 4. It serves an additional purpose here, giving an additional viewpoint on PS and DD over a range of times not limited to the shortand long-time limits. This is particularly useful for observing crossovers in fidelity between protocols. For example, while DD+PS yields the highest fidelity for both protocols at short times (one repetition), PS is generally better suited for periods of long state preservation. The transition in preferred protocol arises due to apparent steady-state behavior in the fidelity that is inconsistent with the completely mixed state. In fact, it is more consistent with a convergence towards a partial symmetric subspace, most notably in the case of the DFS₃ code. Further analysis is required to clarify this behavior.

Appendix J. Logical qubit fidelity and qubit variability

In the main text, we showcase demonstrations that provide evidence of logical encodings outperforming physical qubits via DFS codes combined with error detection and suppression. In sections 4.1 and 4.2, data is shown for specific subsets of qubits on Manila and Montreal. In this section, we show that the behavior observed from these devices is not limited to those subsets; it can also be found in other qubit configurations.

J.1. One logical qubit

First, we focus on the single logical qubit case discussed in section 4.1. The results shown in figure 4 are for the qubit mapping $(q_0, q_1, q_2) = (3, 4, 2)$, following the qubit mapping shown in figure 6. While this subset of qubits yields the highest fidelity for the logical protection protocols, it is not the only subset that conveys an advantage from logical encoding. In figure 16, results are shown for two additional qubit configurations (a) $(q_0, q_1, q_2) = (3, 2, 4)$ and (b) $(q_0, q_1, q_2) = (2, 3, 1)$; see figure 10 for device topology. Average qubit fidelity is determined by bootstrapping over the set of 20 states discussed in section 4.1. Mean fidelities and CIs are determined from one realization of the demonstration performed on 20 October, 2022. Note that in both cases, the DFS encoding, DD, and PS together yield higher fidelities and slower fidelity decay rates than XY4 alone. Thus, empirical findings suggest that the relative improvements from the DFS protocol are robust to variability in qubit characteristics.

J.2. Multiple logical qubits

We further illustrate the robustness of the DFS code through additional studies of the time-averaged fidelity as a function of the number of logical qubits. In figure 17, the time-averaged fidelity in the short-time limit is shown for two additional configurations of physical qubits outlined in table 7. Panels (a) and (b) display results for configurations 2 and 3, respectively, with configuration 1 shown in the main text (figure 5). Each panel contains a comparison between the physical DD and logical DFS₂+DD (with PS) protocols outlined in section 4.2. In both cases, the logical encoding performs similarly or somewhat better than physical-qubit DD, consistent with the results shown in the main text.

Appendix K. Time-averaged fidelity at different integration times

In the main text, results were shown for the time-averaged fidelity with an integration time equivalent to one DFS₂+DD repetition, including encoding and decoding time. In this section, we consider additional integration times and examine the efficacy of each logical protocol. In figure 18, the DFS₂ and DFS₃ codes are compared against physical encoding schemes

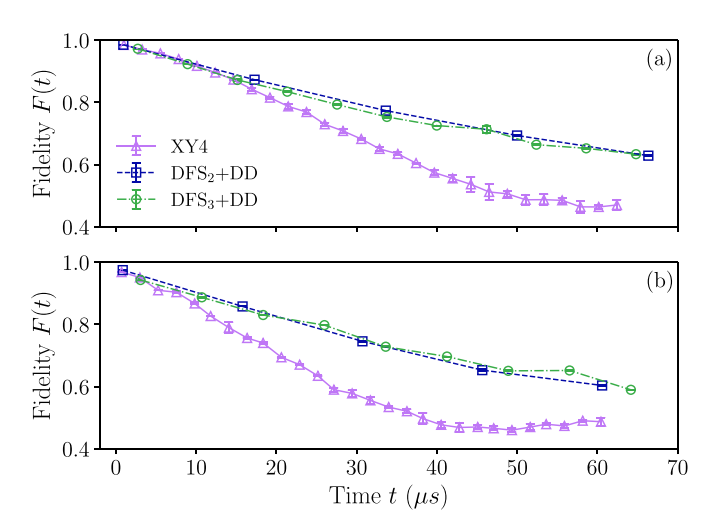


Figure 16. State-averaged fidelity as a function of time for two different qubit mappings on Manila. Panel (a) shows results for XY4, DFS₂+DD, and DFS₃+DD for $(q_0,q_1,q_2)=(3,2,4)$. Similar results are shown in panel (b) for $(q_0,q_1,q_2)=(2,3,1)$. Means (data points) and CIs are estimated from bootstrapping over one demonstration performed on 20 October, 2022, using 8000 shots. In both cases, logical encodings used in conjunction with DD and PS yield higher fidelity and slower fidelity decay than DD alone. Thus, the success of the protocol is independent of the qubit configuration.

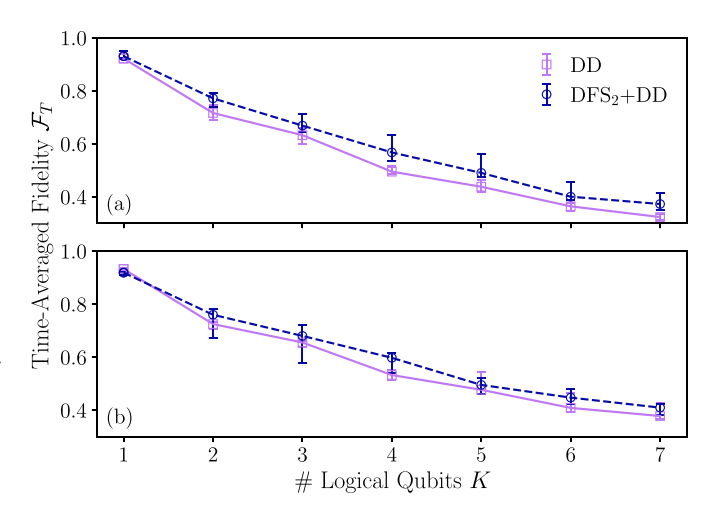


Figure 17. Time-averaged fidelity versus the number of logical qubits for distinct physical qubits configurations on Montreal. Panels (a) and (b) show comparisons for configurations 2 and 3 (table 7), respectively. The DD and DFS₂+DD protocols used for the comparison are equivalent to those described in section 4.2. In both cases, DFS₂+DD performs similarly or better than physical DD alone. Data is processed using bootstrapping to estimate means and CIs (error bars). Bootstrapping is performed over five realizations of the demonstration that were collected from 20–22 October, 2022, each using 8000 shots.

in the long-time limit in panels (a) and (b). Panel (c) compares the DFS $_3$ code to physical encodings for an integration time of one DFS $_3$ +DD repetition with encoding and decoding. As in the main text, all logical protocols utilize PS.

Longer integration time lowers the fidelity. This is particularly true for both the physical DD and DFS₂+DD protocols.

Table 7. Logical qubit configurations for DFS protocol performed on IBMQP Montreal. Each pair (q_0, q_1) denotes a logical qubit, with q_i designating the qubit number based on the hardware topology graph shown in figure 10. Results for configuration 1 are shown in figure 5, while results for 2 and 3 are given in figure 17.

Configuration	Logical Qubits
1	(15,18),(10,12),(4,7),(13,14),(11,8),(16,19),(5,3)
2	(22,25),(20,19),(24,23),(21,18),(15,12),(13,14),(11,8)
3	(4,1),(2,3),(10,7),(5,8),(15,12),(11,14),(17,18)

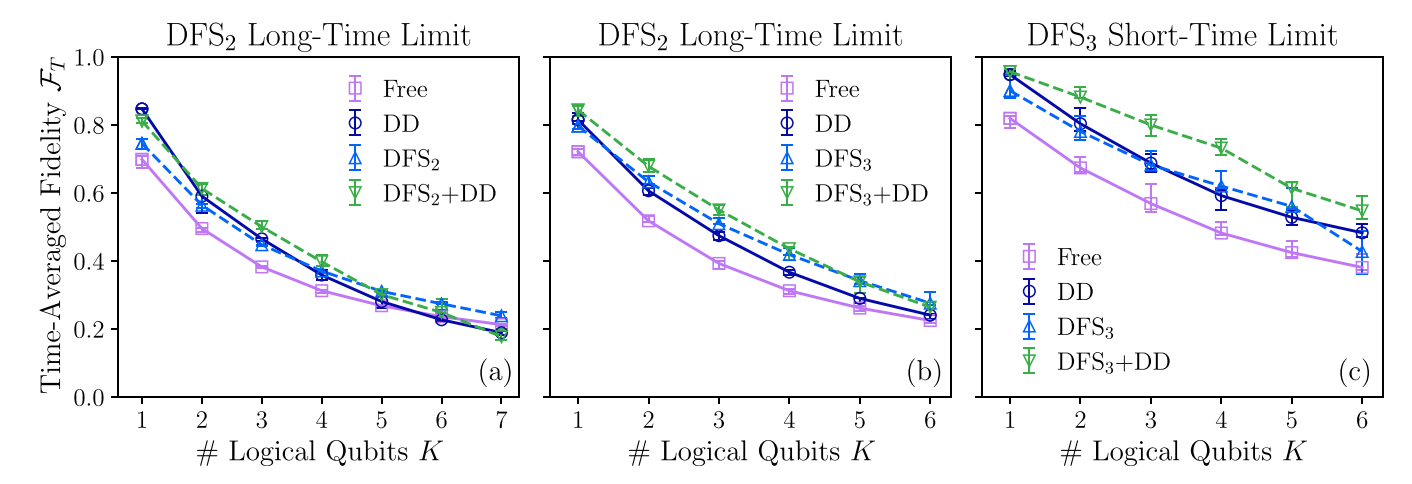


Figure 18. Time-averaged fidelity as a function of the number of logical qubits for different integration times. Comparisons between physical and logical protocols in the long-time limit (i.e. 3 repetitions of the DFS $_2$ +DD sequence) are shown in panels (a) and (b) for the DFS $_2$ and DFS $_3$ code, respectively. Physical (solid lines) and logical (dashed lines) protocols are described in section 4.2. In both cases, the advantage of the logical protocols is observed, particularly when incorporating DD and PS; this is most notable for the DFS $_3$ code. In panel (c), the DFS $_3$ code again exhibits an advantage over physical encoding, but for a total integration time of one DFS $_3$ +DD repetition. Data shown here was collected concurrently with the data used to produce figure 5 and therefore, follows the same data collection and processing practices.

Reduction in fidelity is accompanied by near equivalent performance among both DD-based protocols. Alternatively, the DFS₂ without DD exhibits improvements in this regime such that it begins to outperform all protocols for K > 5. The steady-state behavior observed in figure 15 in the long-time limit ultimately explains this crossover in performance.

PS continues to be an essential part of the DFS₃ protocol outperforming physical qubit error suppression. Both DFS₃ and DFS₃+DD achieve a higher fidelity than DD alone, with the advantage of the DFS₃ increasing with K. The performance improvement is so significant that both the DFS₃ and DFS₃+DD protocols perform nearly identically for K > 5.

Lastly, we comment on an additional short-time limit scenario relative to the DFS₃ code. The main text defines the short-time limit as one cycle of the DFS₂+DD sequence or approximately two cycles of the DFS₃+DD sequence. Here, we consider an integration time of one DFS₃+DD sequence, with results of this comparison shown in figure 18(c). The result is a more pronounced disparity between the physical and logical protocols. The DFS₃ code achieves fidelities nearly equivalent to DD, while the DFS₃+DD protocol yields a maximum improvement in \mathcal{F}_T of 23.6% over DD. The success of both protocols further justifies employing passive QEC codes as a viable logical encoding option for near-term devices.

ORCID iDs

Gregory Quiroz https://orcid.org/0000-0003-4329-1445

Devon Williams https://orcid.org/0000-0002-8386-0051

Daniel Lidar https://orcid.org/0000-0002-1671-1515

References

- [1] Lidar D A and Brun T A (eds) 2013 *Quantum Error Correction* (Cambridge University Press)
- [2] Viola L and Lloyd S 1998 Dynamical suppression of decoherence in two-state quantum systems *Phys. Rev.* A 58 2733–44
- [3] Viola L, Knill E and Lloyd S 1999 Dynamical decoupling of open quantum systems *Phys. Rev. Lett.* **82** 2417
- [4] Zanardi P 1999 Symmetrizing evolutions *Phys. Lett.* A 258 77–82
- [5] Gordon G, Kurizki G and Lidar D A 2008 Optimal dynamical decoherence control of a qubit *Phys. Rev. Lett.* 101 010403
- [6] Suter D and Álvarez G A 2016 Colloquium: Protecting quantum information against environmental noise *Rev. Mod. Phys.* 88 041001
- [7] Shor P W 1995 Scheme for reducing decoherence in quantum computer memory *Phys. Rev.* A 52 R2493
- [8] Steane A M 1996 Error correcting codes in quantum theory Phys. Rev. Lett. 77 793–7

- [9] Gottesman D 1996 Class of quantum error-correcting codes saturating the quantum hamming bound *Phys. Rev.* A 54 1862
- [10] Gaitan F 2008 Quantum Error Correction and Fault Tolerant Quantum Computing (Taylor & Francis Group)
- [11] Alicki R 1988 Limited thermalization for the Markov mean-field model of *N* atoms in thermal field *Physica* A **150** 455–61
- [12] Palma G M, Suominen K-A and Ekert A K 1996 Quantum computers and dissipation *Proc. R. Soc.* A 452 567
- [13] Zanardi P and Rasetti M 1997 Noiseless quantum codes *Phys. Rev. Lett.* **79** 3306–9
- [14] Duan L-M and Guo G-C 1997 Preserving coherence in quantum computation by pairing quantum bits *Phys. Rev. Lett.* **79** 1953–6
- [15] Lidar D A, Chuang I L and Birgitta Whaley K 1998 Decoherence-free subspaces for quantum computation Phys. Rev. Lett. 81 2594
- [16] Knill E, Laflamme R and Viola L 2000 Theory of quantum error correction for general noise *Phys. Rev. Lett.* 84 2525–8
- [17] Zanardi P 2000 Stabilizing quantum information Phys. Rev. A 63 012301
- [18] Cai Z, Babbush R, Benjamin S C, Endo S, Huggins W J, Ying Li, McClean J R and O'Brien T E 2022 Quantum error mitigation (arXiv:2210.00921)
- [19] Lidar D A, Bacon D and Whaley K B 1999 Concatenating decoherence-free subspaces with quantum error correcting codes *Phys. Rev. Lett.* 82 4556–9
- [20] Lidar D A, Bacon D, Kempe J and Birgitta Whaley K 2000 Protecting quantum information encoded in decoherence-free states against exchange errors *Phys. Rev.* A 61 052307
- [21] Viola L, Knill E and Lloyd S 2000 Dynamical generation of noiseless quantum subsystems *Phys. Rev. Lett.* 85 3520–3
- [22] Alber G, Beth T, Charnes C, Delgado A, Grassl M and Mussinger M 2001 Stabilizing distinguishable qubits against spontaneous decay by detected-jump correcting quantum codes *Phys. Rev. Lett.* 86 4402–5
- [23] Alber G, Beth T, Charnes C, Delgado A, Grassl M and Mussinger M 2003 Detected-jump-error-correcting quantum codes, quantum error designs and quantum computation *Phys. Rev.* A 68 012316
- [24] Khodjasteh K and Lidar D A 2002 Universal fault-tolerant quantum computation in the presence of spontaneous emission and collective dephasing *Phys. Rev. Lett.* 89 197904
- [25] Khodjasteh K and Lidar D A 2003 Quantum computing in the presence of spontaneous emission by a combined dynamical decoupling and quantum-error-correction strategy *Phys. Rev.* A 68 022322 Khodjasteh K and Lidar D A 2005 *ibid, Phys. Rev.* A 72 029905 (erratum)
- [26] Ng H K, Lidar D A and Preskill J 2011 Combining dynamical decoupling with fault-tolerant quantum computation *Phys. Rev.* A 84 012305
- [27] Paz-Silva G A and Lidar D A 2013 Optimally combining dynamical decoupling and quantum error correction *Sci. Rep.* 3 1530
- [28] Campbell E T, Terhal B M and Vuillot C 2017 Roads towards fault-tolerant universal quantum computation *Nature* 549 172
- [29] Dumitrescu E F, McCaskey A J, Hagen G, Jansen G R, Morris T, Papenbrock T, Pooser R, Dean D, and Lougovski P 2018 Cloud quantum computing of an atomic nucleus *Phys. Rev. Lett.* 120 210501
- [30] Kandala A, Temme K, Córcoles A D, Mezzacapo A, Chow J M and Gambetta J M 2019 Error mitigation extends the computational reach of a noisy quantum processor *Nature* 567 491–5

- [31] Kim Y, Wood C J, Yoder T J, Merkel S T, Gambetta J M, Temme K and Kandala A 2023 Scalable error mitigation for noisy quantum circuits produces competitive expectation values *Nat. Phys.* 19 752–9
- [32] Pokharel B and Lidar D A 2023 Demonstration of algorithmic quantum speedup *Phys. Rev. Lett.* 130 210602
- [33] Singkanipa P, Kasatkin V, Zhou Z, Quiroz G and Lidar D A 2024 Demonstration of algorithmic quantum speedup for an abelian hidden subgroup problem (arXiv:2401.07934)
- [34] Carr H Y and Purcell E M 1954 Effects of diffusion on free precession in nuclear magnetic resonance experiments *Phys. Rev.* 94 630–8
- [35] Meiboom S and Gill D 1958 Modified spin-echo method for measuring nuclear relaxation times *Rev. Sci. Instrum.* 29 688–91
- [36] Haeberlen U and Waugh J S 1968 Coherent averaging effects in magnetic resonance *Phys. Rev.* 175 453
- [37] Biercuk M J, Uys H, VanDevender A P, Shiga N, Itano W M and Bollinger J J 2009 Experimental Uhrig dynamical decoupling using trapped ions *Phys. Rev.* A 79 062324
- [38] Biercuk M J, Uys H, VanDevender A P, Shiga N, Itano W M and Bollinger J J 2009 Optimized dynamical decoupling in a model quantum memory *Nature* **458** 996–1000
- [39] Sagi Y, Almog I and Davidson N 2010 Process tomography of dynamical decoupling in a dense cold atomic ensemble *Phys. Rev. Lett.* 105 053201
- [40] Naydenov B, Dolde F, Hall L T, Shin C, Fedder H, Hollenberg L C L, Jelezko F and Wrachtrup J 2011 Dynamical decoupling of a single-electron spin at room temperature *Phys. Rev.* B 83 081201
- [41] van der Sar T, Wang Z H, Blok M S, Bernien H, Taminiau T H, Toyli D M, Lidar D A, Awschalom D D, Hanson R and Dobrovitski V V 2012 Decoherence-protected quantum gates for a hybrid solid-state spin register *Nature* 484 82–86
- [42] Souza A M, Álvarez G A and Suter D 2012 Robust dynamical decoupling *Phil. Trans. R. Soc.* A **370** 4748–69
- [43] Pokharel B, Anand N, Fortman B and Lidar D A 2018 Demonstration of fidelity improvement using dynamical decoupling with superconducting qubits *Phys. Rev. Lett.* 121 220502
- [44] Jurcevic P et al 2021 Demonstration of quantum volume 64 on a superconducting quantum computing system Quantum Sci. Technol. 6 025020
- [45] Aharony S, Akerman N, Ozeri R, Perez G, Savoray I and Shaniv R 2021 Constraining rapidly oscillating scalar dark matter using dynamic decoupling *Phys. Rev.* D 103 075017
- [46] Tripathi V, Chen H, Khezri M, Yip K-W, Levenson-Falk E and Lidar D A 2022 Suppression of Crosstalk in Superconducting Qubits Using Dynamical Decoupling Phys. Rev. Appl. 18 024068
- [47] Ezzell N, Pokharel B, Tewala L, Quiroz G and Lidar D A 2023 Dynamical decoupling for superconducting qubits: a performance survey *Phys. Rev. Appl.* 20 064027
- [48] Zhou Z, Sitler R, Oda Y, Schultz K and Quiroz G 2023 Quantum crosstalk robust quantum control *Phys. Rev. Lett.* 131 210802
- [49] Boulant N, Viola L, Fortunato E M and Cory D G 2005 Experimental implementation of a concatenated quantum error-correcting code *Phys. Rev. Lett.* 94 130501
- [50] Harper R and Flammia S T 2019 Fault-tolerant logical gates in the IBM quantum experience *Phys. Rev. Lett.* 122 080504
- [51] Kraglund Andersen C K, Remm A, Lazar S, Krinner S, Lacroix N, Norris G J, Gabureac M, Eichler C and Wallraff A 2020 Repeated quantum error detection in a surface code *Nat. Phys.* 16 875–80
- [52] Chen Z et al 2021 Exponential suppression of bit or phase errors with cyclic error correction Nature 595 383–7

- [53] Krinner S et al 2022 Realizing repeated quantum error correction in a distance-three surface code Nature 605 669-74
- [54] Sivak V V et al 2023 Real-time quantum error correction beyond break-even Nature 616 50–55
- [55] Miao K C, McEwen M, Atalaya J, Kafri D, Pryadko L P, Bengtsson A, Opremcak A, Satzinger K J, Chen Z and Klimov P V 2022 Overcoming leakage in scalable quantum error correction (arXiv:2211.04728)
- [56] Acharya R *et al* 2023 Suppressing quantum errors by scaling a surface code logical qubit *Nature* **614** 676
- [57] Urbanek M, Nachman B and de Jong W A 2020 Error detection on quantum computers improving the accuracy of chemical calculations *Phys. Rev.* A 102 022427
- [58] Postler L, Butt F, Pogorelov I, Marciniak C D, Heußen S, Blatt R, Schindler P, Rispler M, Müller M and Monz T 2023 Demonstration of fault-tolerant Steane quantum error correction (arXiv:2312.09745)
- [59] Bluvstein D, Evered S J, Geim A A, Sophie H Li, Zhou H, Manovitz T, Ebadi S, Cain M, Kalinowski M, Hangleiter D et al 2023 Logical quantum processor based on reconfigurable atom arrays Nature 626 58–65
- [60] Tuladhar A S, Bhattarai A, Bimali S, Pokharel B, Pradhan S, Shrestha A and Acharya R 2022 Better-than-classical Grover search via quantum error detection and suppression JNMA 60 857–60
- [61] Kwiat P G, Berglund A J, Altepeter J B and White A G 2000 Experimental verification of decoherence-free subspaces Science 290 498–501
- [62] Viola L, Fortunato E M, Pravia M A, Knill E, Laflamme R and Cory D G 2001 Experimental realization of noiseless subsystems for quantum information processing *Science* 293 2059–63
- [63] Ollerenshaw J E, Lidar D A and Kay L E 2003 Magnetic resonance realization of decoherence-free quantum computation *Phys. Rev. Lett.* 91 217904
- [64] Mohseni M, Lundeen J S, Resch K J and Steinberg A M 2003 Experimental application of decoherence-free subspaces in an optical quantum-computing algorithm *Phys. Rev. Lett.* 91 187903
- [65] Fortunato E M, Viola L, Pravia M A, Knill E, Laflamme R, Havel T F and Cory D G 2003 Exploring noiseless subsystems via nuclear magnetic resonance *Phys. Rev.* A 67 062303
- [66] Altepeter J B, Hadley P G, Wendelken S M, Berglund A J and Kwiat P G 2004 Experimental investigation of a two-qubit decoherence-free subspace *Phys. Rev. Lett.* 92 147901
- [67] Pushin D A, Huber M G, Arif M and Cory D G 2011 Experimental realization of decoherence-free subspace in neutron interferometry *Phys. Rev. Lett.* 107 150401
- [68] Preskill J 2018 Quantum computing in the NISQ era and beyond Quantum 2 79
- [69] Wu L-A and Lidar D A 2002 Creating decoherence-free subspaces using strong and fast pulses *Phys. Rev. Lett.* 88 207902
- [70] Wu L-A, Byrd M S and Lidar D A 2002 Efficient universal leakage elimination for physical and encoded qubits *Phys. Rev. Lett.* 89 127901
- [71] Byrd M S and Lidar D A 2002 Comprehensive encoding and decoupling solution to problems of decoherence and design in solid-state quantum computing *Phys. Rev. Lett.* 89 047901
- [72] Lidar D A and Wu L-A 2003 Encoded recoupling and decoupling: An alternative to quantum error-correcting codes applied to trapped-ion quantum computation *Phys. Rev.* A 67 032313

- [73] Lidar D A and Lian-Ao W 2003 Quantum computers and decoherence: exorcising the demon from the machine *Proc.* SPIE 5115 256–70
- [74] Byrd M S, Lidar D A, Wu L-A and Zanardi P 2005 Universal leakage elimination *Phys. Rev.* A **71** 052301
- [75] Fong B H and Wandzura S M 2011 Universal quantum computation and leakage reduction in the 3-qubit decoherence free subsystem *Quantum Inf. Comput.* 11 1003
- [76] West J R and Fong B H 2012 Exchange-only dynamical decoupling in the three-qubit decoherence free subsystem *New J. Phys.* 14 083002
- [77] Mena López A and Lian-Ao W 2023 Protectability of IBMQ qubits by dynamical decoupling technique *Symmetry* 15 62
- [78] Han J-X, Zhang J, Xue G-M, Haifeng Y and Long G 2024 Protecting logical qubits with dynamical decoupling (arXiv:2402.05604)
- [79] Kempe J, Bacon D, Lidar D A, Lidar D A and Whaley K B 2001 Theory of decoherence-free fault-tolerant universal quantum computation *Phys. Rev.* A 63 042307
- [80] Medford J, Beil J, Taylor J M, Taylor J M, Rashba E I, Lu H, Gossard and Marcus C M 2013 Quantum-dot-based resonant exchange qubit *Phys. Rev. Lett.* 111 050501
- [81] Taylor J M, Srinivasa V and Medford J 2013 Electrically protected resonant exchange qubits in triple quantum dots *Phys. Rev. Lett.* 111 050502
- [82] Burkard G, Ladd T D, Pan A, Nichol J M and Petta J R 2023 Semiconductor spin qubits Rev. Mod. Phys. 95 025003
- [83] Fortunato E M, Viola L, Hodges J, Teklemariam G and Cory D G 2002 Implementation of universal control on a decoherence-free qubit New J. Phys. 4 5
- [84] Daniel A L 2014 Review of Decoherence-Free Subspaces, Noiseless Subsystems and Dynamical Decoupling (Wiley) pp 295–354
- [85] Yang C-P and Gea-Banacloche J 2001 Three-qubit quantum error-correction scheme for collective decoherence *Phys. Rev.* A 63 022311
- [86] Weinstein A J et al 2023 Universal logic with encoded spin qubits in silicon Nature 615 817–22
- [87] Bacon D, Kempe J, DiVincenzo D P, Lidar D A and Whaley K B 2001 Encoded universality in physical implementations of a quantum computer *Proc. 1st Int. Conf. on Experimental Implementations of Quantum Computation (Sydney, Australia)* ed R G Clark (Rinton) p 257
- [88] Kempe J, Bacon D, DiVincenzo D P and Whaley K B 2001 Encoded universality from a single physical interaction *Quantum Inf. Comput.* 1 33
- [89] DiVincenzo D P, Bacon D, Kempe J, Burkard G and Whaley K B 2000 Universal quantum computation with the exchange interaction *Nature* 408 339–42
- [90] Nielsen M A and Chuang I L 2011 Quantum Computation and Quantum Information: 10th Anniversary edn 10th edn (Cambridge University Press)
- [91] Xia Y, Uhrig G S and Lidar D A 2011 Rigorous performance bounds for quadratic and nested dynamical decoupling *Phys. Rev.* A 84 062332
- [92] Zhang J, Zhou Z-Y, Wu L-A and You J Q 2019 Protection of logical qubits via optimal state transfers *Phys. Rev. Appl.* 11 044023
- [93] McKay D C *et al* 2018 Qiskit Backend Specifications for OpenQASM and OpenPulse Experiments (arXiv:1809. 03452 [quant-ph])
- [94] Tripathi V, Preetha G S, Pandey A K and Vijay P 2023 Modeling low- and high-frequency noise in transmon qubits

- with resource-efficient measurement *Vector Borne Zoonotic Dis.* 23 113–8
- [95] Oda Y, Shehab O and Quiroz G 2023 Noise modeling of the IBM quantum platform 2023 IEEE Int. Conf. on Quantum Computing and Engineering (QCE) vol 2 (IEEE) pp 219–22
- [96] Niu S and Todri-Sanial A 2022 Analyzing strategies for dynamical decoupling insertion on IBM quantum computer (arXiv:2204.14251)
- [97] Li C-K, Nakahara M, Poon Y-T, Sze N-S and Tomita H 2011 Recursive encoding and decoding of the noiseless subsystem and decoherence-free subspace *Phys. Rev.* A 84 044301
- [98] Stine R 1989 An introduction to bootstrap methods: Examples and ideas *Sociol. Methods Res.* **18** 243–91
- [99] Stoica P and Selen Y 2004 Model-order selection: a review of information criterion rules *IEEE Signal Process. Mag.* 21 36–47